CANCER RESEARCH COMMUNICATIONS

AACR American Association for Cancer Research

RESEARCH ARTICLE https://doi.org/10.1158/2767-9764.CRC-22-0396 OPEN ACCESS

Ultra High-plex Spatial Proteogenomic Investigation of Giant Cell Glioblastoma Multiforme Immune Infiltrates Reveals Distinct Protein and RNA Expression Profiles

Shilah A. Bonnett[1], Alyssa B. Rosenbloom[1], Giang T. Ong[1], Mark Conner[1], Aric B.E. Rininger[1], Daniel Newhouse[1], Felicia New[1], Chi Q. Phan[1], Saskia Ilcisin[1], Hiromi Sato[1], John S. Lyssand[1], Gary Geiss[1], and Joseph M. Beechem[1]

ABSTRACT

A deeper understanding of complex biological processes, including tumor development and immune response, requires ultra high-plex, spatial interrogation of multiple "omes". Here we present the development and implementation of a novel spatial proteogenomic (SPG) assay on the GeoMx Digital Spatial Profiler platform with next-generation sequencing readout that enables ultra high-plex digital quantitation of proteins (>100-plex) and RNA (whole transcriptome, >18,000-plex) from a single formalin-fixed paraffin-embedded (FFPE) sample. This study highlighted the high concordance, $R > 0.85$ and <15% change in sensitivity between the SPG assay and the single-analyte assays on various cell lines and tissues from human and mouse. Furthermore, we demonstrate that the SPG assay was reproducible across multiple users. When used in conjunction with advanced cellular neighborhood segmentation, distinct immune or tumor RNA and protein targets were spatially resolved within individual cell subpopulations in human colorectal cancer and non–small cell lung cancer. We used the SPG assay to interrogate 23 different glioblastoma multiforme (GBM) samples across four pathologies. The study revealed distinct clustering of both RNA and protein based on pathology and anatomic location. The in-depth investigation of giant cell glioblastoma multiforme (gcGBM) revealed distinct protein and RNA expression profiles compared with that of the more common GBM. More importantly, the use of spatial proteogenomics allowed simultaneous interrogation of critical protein posttranslational modifications alongside whole transcriptomic profiles within the same distinct cellular neighborhoods.

Significance: We describe ultra high-plex spatial proteogenomics; profiling whole transcriptome and high-plex proteomics on a single FFPE tissue section with spatial resolution. Investigation of gcGBM versus GBM revealed distinct protein and RNA expression profiles.

Introduction

The advancement of spatially resolved, multiplex proteomic and transcriptomic technologies has revolutionized and redefined the approaches to complex biological questions pertaining to tissue heterogeneity, tumor microenvironments, cellular interactions, cellular diversity, and therapeutic response (1). These spatial technologies, including the GeoMx Digital Spatial Profiler (DSP), can yield spatially resolved proteomic and transcriptomic datasets from formalin-fixed paraffin-embedded (FFPE) or fresh frozen samples. Most of these approaches are specific toward generating either proteomic or transcriptomic datasets. Multiple studies have demonstrated a poor correlation between RNA expression and protein abundance in samples when each analyte is profiled, with the most egregious of cases often owing to target- or tissue-specific posttranscriptional regulation (2–5). Despite our current understanding of the variety of mechanisms surrounding transcriptional and translational regulation, target turnover, posttranslational protein modifications, and protein activity, RNA is still the primary analyte of choice in highly multiplexed studies. A workflow that accurately measures RNA and protein simultaneously within a single sample and spatial context is critical to a fuller understanding of the global state of the cell.

Previously, to understand proteomic and transcriptomic relationships, researchers would acquire individual analyte-specific datasets, often employing different technologies, and computationally integrate the data using various multiomic approaches (refs. 6–9; Fig. 1A). While this workflow provides a deeper understanding of the biological system under study, the potentially confounding variables associated with variation stemming from employing multiple technologies, section-to-section variability, or precisely matching

[1]NanoString Technologies, Seattle, Washington.

Corresponding Author: Joseph M. Beechem, NanoString Technologies, 530 Fairview Ave N, Seattle, WA 98109. Phone: 206-432-8823; E-mail: jbeechem@nanostring.com

doi: 10.1158/2767-9764.CRC-22-0396

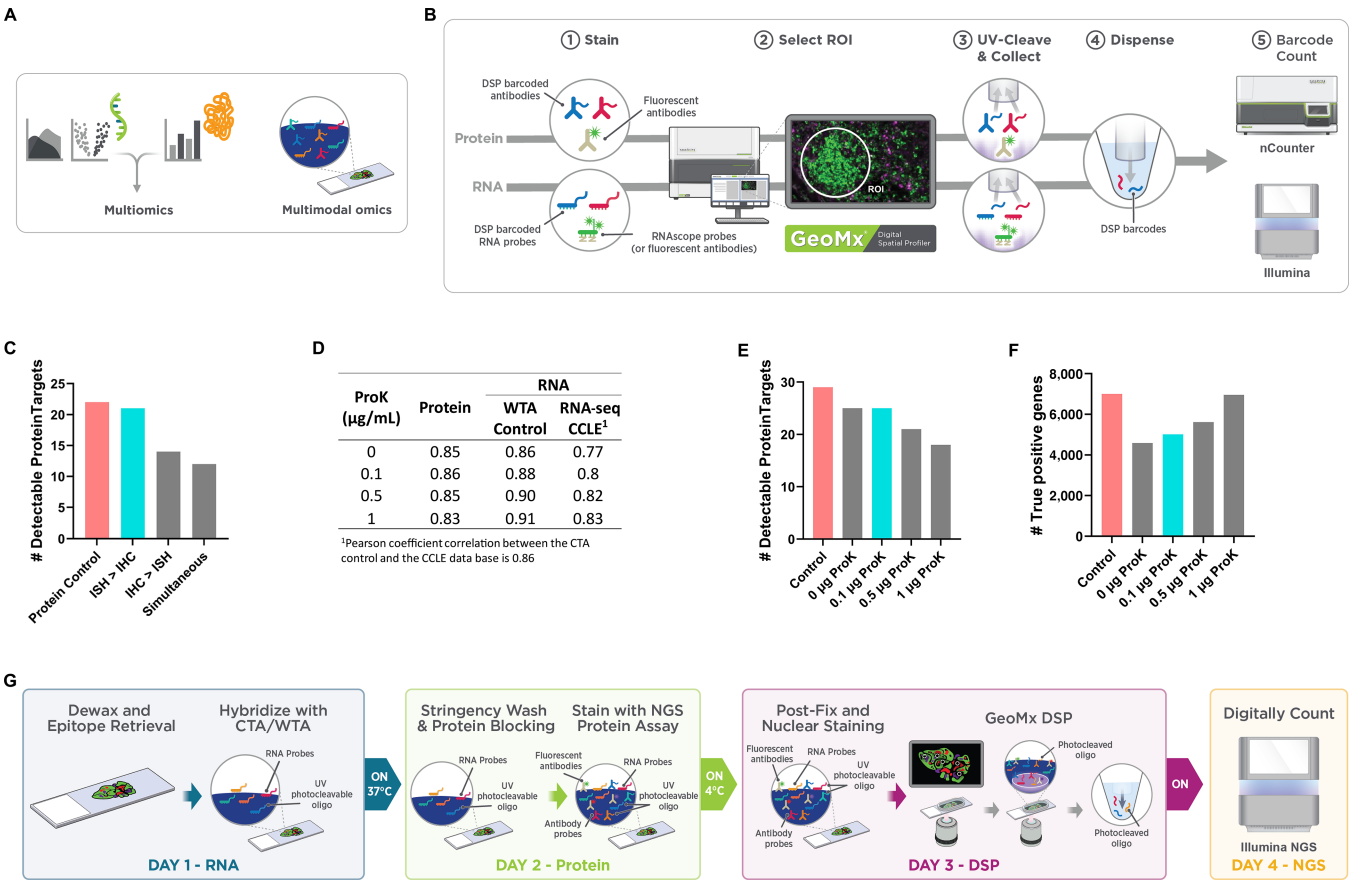

FIGURE 1 Technical development of the SPG assay. **A,** Current proteogenomic approaches are multiomic which entails the integration of individual -omic datasets and multimodal omics which involves the simultaneous, codetection of multiple "omes" in a single sample. **B,** Commercially available GeoMx Assays currently enable high-plex, spatially resolved protein and RNA targets on individual tissue sections with nCounter or NGS quantitative readout. **C,** Assessment of staining order on the number of protein targets above detection threshold (SNR $\geq$ 3). FFPE cell line, A431CA, was stained with GeoMx Protein assays (59-plex) for nCounter readout and mock RNA probe (Buffer R only). **D,** Assessment of varying ProK on the performance of the SPG assay. A 45-CPA was stained with 59-plex GeoMx NGS Protein modules (59-plex) and the GeoMx Whole Transcriptome Atlas (WTA) under proteogenomic and standard assay conditions. **E,** Plots represent the number of targets above the detection threshold for Pearson correlation on $\log_2$-transformed SNR data between the proteogenomic assay and the single-analyte controls along with the CCLE RNA-seq database. Circular ROIs of 200 µm diameter were selected for detailed molecular profiling with the GeoMx DSP. The signal was averaged across replicate AOIs and the SNR was calculated. Protein (SNR $\geq$ 3; **E**) and true positives (**F**) in detectable WTA targets. **G,** GeoMx SPG workflow enables multimodal omic profiling on a single slide.

regions of interest (ROI) across multiple slides must be taken into consideration when analyzing and interpreting the data. To control or eliminate these potentially confounding technical variables, multimodal omics, defined as the simultaneous codetection of multiple analytes ("omes") in a single sample, serves as an advantageous alternative approach (refs. 10–13; bioRxiv 2022.04.01.486788). In the emerging spatial biology field, there has been a growing interest in the development of novel multimodal omic protocols to detect RNA transcript levels and protein abundance within a single sample while maintaining the spatial context within a tissue. These novel multimodal omic datasets of protein and DNA or RNA have been termed "spatial proteogenomics." While mass spectrometry–based proteomics is the most widely used approach for proteogenomic analysis, which enables the measurement of >1,000 protein targets, antibody-based approaches usually involve lower plex (<300 targets; refs. 12–17). However, until recently, spatial proteogenomic (SPG) protocols with ultrahigh-plex, simultaneous codetection of analytes have not been available (refs. 11–13, 18–27; bioRxiv 2022.04.01.486788). Many of the protocols combine high-plex RNA with up to four fluorescent antibodies utilized as morphology markers.

The GeoMx DSP enables spatially resolved, high-plex digital quantitation of proteins (>100-plex) and RNA (whole transcriptome, >18,000-plex) from human and mouse tissues (28–31). Previous work has detailed proteomic or transcriptomic single-analyte workflows using the GeoMx DSP technology with unique affinity reagents (antibodies for protein or ISH probes for RNA) coupled to photocleavable oligonucleotide barcodes (refs. 28, 29, 31; Fig. 1B). Tissue samples are incubated with one of these affinity reagents, and oligonucleotide barcodes are precisely liberated from an area of interest (AOI) with UV light exposure. The released barcodes are then collected for quantification with next-generation sequencing (NGS). While the assays were developed for single-analyte analysis, there is no fundamental technical barrier to concurrently profile protein and RNA targets on a single sample. However, the

divergent sample preparation protocols for RNA and protein would hinder the concurrent profiling of both analytes. Here we introduce a novel GeoMx DSP SPG workflow that allows for the simultaneous codetection and quantification of RNA transcripts and protein abundance in a defined cell population within individual FFPE mouse and human tissues, using oligonucleotide-barcoded affinity reagents and the GeoMx DSP platform and Illumina NGS readout. We demonstrate the performance of the assay on various cell lines and tissues and highlight its use in a biological context on various glioblastoma multiforme (GBM) samples including giant cell glioblastoma multiforme (gcGBM).

Materials and Methods

All experiments were carried out using reagents recommended or provided by NanoString Technologies and are summarized in Supplementary Tables S1 and S2, respectively. A list of antibodies making up each of the Human and Mouse GeoMx Protein Modules are summarized in Supplementary Tables S3 and S4, respectively. All reagents and instruments are for Research Use Only and not for use in diagnostic procedures.

FFPE Samples—Cell Lines

Sections of FFPE cell pellet arrays (CPA) and tissues, 5 μm in thickness, were used in these studies. Two custom CPAs consisting of 11 and 45 human cell lines were generated by Acepix. Each base cell line was procured from one of three biobanks (ATCC, Deutsche Sammlung von Mikrooganism and Zellkulturen [DSMZ], or ECACC) and cell lines with stable overexpression of selected targets were purchased from vendors (CrownBio). Base cell lines were thawed, expanded, and embedded into FFPE between passages 2 and 4, within 8 weeks of thawing. *Mycoplasma* testing and cell line authentication were performed by ATCC, DSMZ, European Collection of Animal Cell Cultures (short tandem repeat analysis), or CrownBio (FACS analysis) prior to purchase.

Cell lines stably overexpressing select targets (CrownBio) were authenticated by vendor with FACS analysis of expression of the expected overexpressed target. No *Mycoplasma* testing is described by CrownBio and no additional *Mycoplasma* testing was done by NanoString Technologies or Acepix during cell expansion and FFP-embedding procedures. Passage numbers for each of the above cell lines did not exceed 4.

A431, SH-SY5Y, and SKBR3 cells were thawed, expanded, and treated with Calyculin A (TOCRIS, catalog no. 1336, 100 nmol/L, 30 minutes) prior to fixation and embedding. No additional *Mycoplasma* testing was done by NanoString Technologies or Acepix during cell treatment, expansion, and FFP-embedding procedures. Passage numbers for each of the treated cell lines did not exceed 4.

Cells were FFPE and assembled in the CPAs (Acepix) within 6 months of receipt and/or production from the respective biobanks (ATCC, DSMZ, or ECACC), vendors (CrownBio), and in house treated cell lines (NanoString). The FFPE CPAs were built between 2019 and 2022.

The complete list of cell lines (Biobank, catalog no., RRID) within the CPAs can be found in Supplementary Tables S5 and S6.

FFPE Samples—Tissues

FFPE sections of human colorectal cancer were from either BioChain (catalog no.: T22235090-1) or ProteoGenex (catalog no.: 025562T2). Human FFPE non–small cell lung cancer (NSCLC) was from US BioMax (catalog no.: HuCAT231) or ProteoGenex (catalog no.: 041556T2). Mouse multiorgan tissue microarray (TMA) was from SuperBiochips (catalog no.: ZE1; ICR mice, 8 weeks old) and human brain glioblastoma tissue array was from US Biomax (catalog no.: GL806g).

GeoMx Single-analyte Protein and RNA Assay

For protein only control, slides were manually processed according to the Protein FFPE Manual Slide Preparation Protocol in the GeoMx-NGS Slide Preparation User Manual (MAN-10150) and associated published material (29).

RNA only control slides were processed according to the RNA FFPE BOND RX Slide Preparation Protocol in the GeoMx-NGS Slide Preparation User Manual for FFPE (MAN-10151) and associated published materials (28, 29, 31).

GeoMx SPG Assay Sample Preparation

SPG slides were processed according to the GeoMx DSP SPG Protocol (MAN-10158) and Quick guide (Supplementary Method S1).

GeoMx DSP Experiments—ROI Selection and Collection

For the SPG slides, GeoMx Digital Spatial Profiling was carried out according to GeoMx-DSP SPG Protocol (MAN-10158); whereas the control slides were processed according to GeoMx-NGS DSP Instrument User Manual (MAN-10152) and as described by Merritt and colleagues (29, 31). For CPAs, two geometric ROIs of 200 μm in diameter were profiled per cell line.

Tissue sections were stained with fluorescent morphology markers and nuclear counterstain (Syto-13) to aid in the selection of AOIs. Human colorectal cancer, human NSCLC, and a mouse multiorgan tissue array were stained with the GeoMx Solid Tumor TME Morphology Kit (NanoString, GMX-PRO-MORPH-HST-12 and GMX-RNA-MORPH-HST-FFPE-12, for human and mouse, respectively) to aid in the visualization of immune ($CD45^+$) and epithelial/tumor ($PanCK^+$) enriched regions. Human brain glioblastoma with normal brain TMA was stained with the GeoMx Solid Tumor TME Morphology Kit and anti-GFAP AF647 antibody (astrocytes, Novus Biologicals, NPB2-33184AF647, RRID:AB_2935766).

In human tissues, circular geometric ROIs of 100 μm in diameter were collected for each morphology marker-specific ROI. In the mouse multiorgan array, anatomically distinct regions were selected for specific tissue and then sampled with 100 μm diameter circular geometric ROIs. Two to three regions were selected for each tissue. For each tissue type, ROIs were matched across all test slides under study. An advanced ROI selection strategy (segmentation) was implemented on colorectal cancer, NSCLC, and GBM. For segmentation experiments, circular ROIs of 300 μm in diameter were segmented into marker-specific AOIs using the GeoMx autosegmentation tool (32).

NGS and Data Analysis

Library preparations were carried out according to the GeoMx-DSP SPG Protocol (MAN-10158). Libraries were sequenced on an Illumina NextSeq2000 or NovaSeq6000 according to the manufacturer's instructions.

The resulting FASTQ files were processed along with a modified GeoMx NGS Pipeline config file using the NanoString GeoMx NGS Pipeline v2.0 or v2.3 according to the GeoMx DSP NGS Readout User Manual (MAN-10153). As recommended in MAN-10158, proteogenomic data were processed and analyzed using GeomxTools (v3.1.1; https://github.com/Nanostring-Biostats/GeomxTools/; RRID:SCR_023424) in R separately for the protein and RNA analytes. AOIs with low reads sequenced, low saturation, and low area were removed from analysis.

Limit of Quantification (LoQ) is calculated for raw data based on the distribution of the negative control probes ("NegProbe") and is used as an estimation for the quantifiable limit of gene expression per AOI (31). Using the geometric mean and geometric SD of the negative control probes, LoQ for the *i*th AOI is calculated as follows:

$$\text{LoQ} = \text{geoMean}\left(\text{NegProbe}_i\right) * \text{geoSD}\left(\text{NegProbe}_i\right)^2$$

A gene is considered detected within a specific AOI if its expression is above the LoQ for that AOI. For tissues, AOIs where less than 5% of the genes were above LoQ were removed. Unless stated otherwise, genes were included in the analysis if it was above the LoQ in >15% AOIs profiled in a specific tissue.

For both analytes, the signal-to-noise ratio (SNR) for each target was calculated and used to represent the normalized gene or protein expression in downstream analyses. For RNA, the SNR was calculated by dividing each gene count in an AOI by the geometric mean of the negative probes in that AOI. For protein, the SNR was calculated by dividing the protein count by the geometric mean of the three IgG negative controls (mouse IgG1 and IgG2a, and rabbit IgG).

Advanced analysis was carried out on protein and gene targets with an SNR ≥ 3 and ≥4, respectively. Cluster heatmaps were generated with the pheatmap R package (RRID:SCR_016418). Clustering was carried out on log-transformed scaled counts using the pheatmap "correlation" method. For tissue, differential expression (DE) analysis between different populations of cells was performed for each analyte using a two-sided, unpaired *t* test from rstatix R package (RRID:SCR_021240). The threshold for significance was set at *P* value <0.05 and adjusted for multiple comparisons (or multiple hypothesis testing) using the Benjamini–Hochberg method. The estimated fold changes ($\log_2$FC) in the SNR and *P* values for both analytes were summarized in a single volcano plot using R ggplot2 package (RRID:SCR_014601).

Data Normalization for GBM Studies

Proteogenomic data generated from the GBM studies were processed and analyzed using GeomxTools (v3.1.1) in R separately for the protein and RNA analytes as noted above. For the protein analyte, proteogenomic data underwent SNR normalization using the geometric mean of three IgG negative controls. For RNA, we calculated the LoQ for each AOI and first removed segments where less than 5% of the genes were above LoQ. We then removed genes that were below the LoQ in at least 10% of the AOIs. After segment and gene filtering, the data underwent SNR normalization.

Statistical Analyses for GBM Studies

All analyses were performed in R (v 4.1.2). Uniform Manifold Approximation and Projection (UMAP) plots were generated with normalized expression data using the umap packages (v0.2.8.0; RRID:SCR_018217) using default settings. Coefficients of variation (CV) were calculated for each protein or gene ($CV_g = SD_g/mean_g$). The genes with the highest CVs were filtered and plotted as a heatmap using unsupervised hierarchical clustering based on Pearson distance. Heatmaps were generated using the ComplexHeatmap (33) package (v2.10.0; RRID:SCR_017270).

DE analysis was performed on a per-gene basis where the normalized expression was modeled using a linear mixed-effect model to account for multiple sampling of ROI/AOI segments per tissue. DE was performed using the mixedModelDE function from the GeomxTools package (v3.1.1). DE results were visualized in volcano plots and violin plots using the ggplot2 package (v3.3.6; RRID:SCR_014601). Volcano plots are used to visualize the overall results of DE with estimated fold changes ($\log_2$FC) in the SNR and *P* values plotted for each contrast. Violin plots highlight features of interest and the most differentially expressed genes or proteins in a comparison, visualized using SNR.

Data Availability

All raw and processed data used in this article will be available upon request in writing to the corresponding author.

Results

SPG Assay Development

Multiomic profiling of RNA and Protein generally requires two serial tissue sections (Fig. 1A). Serial sections often include similar, but not identical, cell populations and thus do not provide the optimal measurement of the relationship between gene expression and protein abundance. Therefore, we set out to develop a novel high-plex spatial multimodal assay on the GeoMx DSP platform with NGS readout (Fig. 1A and B), which allows for the simultaneous profiling of high-plex RNA transcripts and proteins from a defined cell population within individual AOI on a single FFPE tissue section. We named this assay the GeoMx Spatial Proteogenomic assay or SPG for short.

For the individual GeoMx NGS Protein assay and GeoMx NGS RNA assay, sample preparation protocols are nearly identical to standard IHC or ISH methodologies, respectively. The GeoMx NGS Protein assay uses a single antigen retrieval process of a slightly acidic heat-induced epitope retrieval (HIER) buffer (pH 6.0) under high pressure. The GeoMx NGS RNA assay uses a two-step, tissue-dependent epitope retrieval process with a basic HIER buffer (pH 9.0) followed by a proteolytic-induced epitope retrieval (PIER) step. Given two analytes that required distinct and disparate antigen retrieval conditions, we first optimized sample treatment conditions compatible with both analytes: staining, epitope retrieval, and Proteinase K (ProK) digestion.

Staining Strategy

Sample preparation for ISH normally involves harsh conditions, such as high salt concentrations and prolonged exposure to formamide at elevated temperatures, all of which may disrupt the antigen–antibody complex and thus reduce protein detection in FFPE tissue samples. To investigate the impact of ISH conditions on protein antigen detection, we first evaluated two sequential staining strategies: ISH staining followed by IHC staining (ISH > IHC) and in the reverse order (IHC > ISH). After implementing both staining steps, slides were subsequently processed on the GeoMx platform. We hypothesized ISH > IHC would result in optimal protein detection when compared with the reverse order. When IHC staining was performed first, followed by ISH, we found a slightly lower correlation ($R = 0.86$) and a 36% decrease in sensitivity when compared with single-analyte protein control (Fig. 1C; Supplementary Fig. S1). In contrast, carrying out ISH first, followed by IHC staining, had only a minor impact on protein correlation ($R = 0.95$) and sensitivity (5% decrease).

We also evaluated a simultaneous strategy, concurrently staining with both antibodies (for IHC) and RNA probes (for ISH) under conditions where formamide was reduced 5-fold. For this experiment, we evaluated the impact of the simultaneous staining conditions on protein detection in absence of RNA probes. While formamide allows for the hybridization to occur at lower temperatures and reduces the nonspecific binding of RNA probes, it can disrupt antibody–antigen interactions, and thus the quality of antibody-based protein detection

(11, 34). With the simultaneous staining strategy, we observed a 45% decrease in protein target detection, indicating disruption of antibody-antigen binding even in the reduced formamide concentration (Fig. 1C; Supplementary Fig. S1). Therefore, we concluded that the optimal strategy for dual detection of RNA and protein targets was sequential staining with ISH followed by IHC.

Impact of Epitope Retrieval Conditions

Next, we sought to identify the optimal epitope retrieval conditions for the SPG assay. The standard GeoMx RNA and Protein assays are designed to perform at opposing HIER conditions, basic and slightly acidic conditions, respectively, whereas the SPG assay workflow calls for a single epitope retrieval condition. To optimize the HIER conditions specifically for the SPG assay, 11 FFPE CPA sections were pretreated under basic or slightly acidic HIER conditions followed by PIER with 1 μg/mL of ProK. The CPA sections provide a uniform set of cells with known RNA expression levels as defined by the Cancer Cell Line Encyclopedia (CCLE) RNA sequencing (RNA-seq) dataset (35). Pretreated sections were then stained in a sequential fashion with the GeoMx Human Cancer Transcriptome Assay (GeoMx CTA; ∼1,800 protein-coding genes) followed by a set of modular GeoMx Human NGS Protein panels (59-plex; Supplementary Table S2). For each cell line, the signal was averaged across biological replicate ROIs and the SNR was calculated for protein and RNA targets. The performance of the SPG assay was compared with the single-analyte assay control slides.

When the SPG assay data on FFPE cell lines were compared with the single-analyte RNA assay controls, we observed a strong correlation ($R > 0.94$) regardless of slightly acidic or basic HIER pretreatment conditions (Supplementary Fig. S2A and S2B). In addition, HIER pretreatment conditions had little impact on the correlation between the SPG assay data and the CCLE RNA-seq data ($R > 0.84$; ref. 35; Supplementary Fig. S2C). From the CCLE RNA-seq dataset, we identified a true set of expressed genes (TPM > 1) that was used to calculate the true positive rate (sensitivity) and false positive rate (FPR, specificity) with respect to assessed RNA targets. The FPR of the SPG assay under basic HIER conditions was <10% (Supplementary Fig. S2D). In contrast, for the assay under slightly acidic HIER conditions, the FPR increased to 30%. The high FPR associated with slightly acidic HIER conditions is consistent with the previous observation: an increase in nonspecific hybridization when epitope retrieval was performed under slightly acidic conditions (31).

The SPG assay was then compared with the single-analyte protein assay from FFPE cell lines. The pretreatment of samples with slightly acidic HIER demonstrated a higher correlation ($R = 0.86$) to the protein assay control than with the basic HIER treatment ($R = 0.77$; Supplementary Fig. S3A and S3B). Thus, the evaluation of epitope retrieval methods indicated the optimal detection of protein under slightly acidic HIER conditions and the optimal detection of RNA under basic conditions, which is consistent with the standard GeoMx single-analyte workflows. While detection sensitivity for protein decreased when slides were pretreated under basic conditions followed by ProK, nonspecific binding for RNA increased under slightly acidic conditions. To move forward, we chose to maintain RNA detection specificity and refine protein sensitivity by titrating ProK concentrations under basic HIER conditions.

Impact of ProK Concentrations

We noted the relatively high concentration of ProK (1 μg/mL) used in the PIER step drove protein target detection loss due to antigen digestion (Supplementary Fig. S3C). Thus, we assessed the effects of ProK concentration under basic HIER on protein and RNA target detection in the SPG assay. To evaluate the effects of various concentrations of ProK, 45 FFPE CPA sections were stained with the GeoMx Human Whole Transcriptome Atlas (GeoMx Human WTA; >18,000 protein-coding genes) probe set and a 59-plex set of GeoMx Human NGS Protein panels. FFPE cell lines were assessed under basic HIER conditions followed by PIER with varying concentrations of ProK. When comparing the single-analyte protein control with the SPG assay, the SNR correlations between these two assays remained relatively strong ($R = 0.83–0.86$; Fig. 1D; Supplementary Fig. S4A–S4D) and FPR remained <10%, regardless of ProK concentrations (Supplementary Fig. S4E). However, the levels of protein target detection significantly decreased (>37%) at ProK concentrations ≥1 μg/mL (Fig. 1E). At 0.1 μg/mL ProK, the number of detected protein targets by the SPG assay was comparable (∼13% decrease in detection) to the single-analyte protein control.

For RNA targets, the correlation between the SPG assay and the RNA single-analyte control was higher when the samples were treated with increased ProK concentrations as expected ($R = 0.86$ for 0 μg/mL ProK, $R = 0.88–0.91$ for 0.1–1.0 μg/mL ProK; Fig. 1D; Supplementary Fig. S5A–S5D). A similar trend was observed when we compared the SPG assay data of RNA targets with the CCLE RNA-seq data ($R = 0.77$ for 0 μg/mL ProK, $R = 0.8–0.83$ for 0.1–1.0 μg/mL ProK; Fig. 1D; Supplementary Fig. S5E). Using the CCLE RNA-seq dataset, we identified a true set of expressed genes (TPM > 1) that was used to calculate the number of true positives. In our analysis, the number of true positives increased with higher concentrations of ProK (Fig. 1F; Supplementary Fig. S5F). These results demonstrate the critical balance between ProK proteolytic digestion and optimal RNA detection. Even at the lowest ProK concentrations, the digestion of critical protein epitopes was detectable. Particularly, the detection of low-abundance protein and RNA targets was the most affected by ProK.

GeoMx SPG Workflow

After optimizing the staining strategy for the SPG assay, including the epitope retrieval conditions and ProK concentrations on sensitivity and specificity for protein and RNA detection, we established the optimal GeoMx SPG workflow. This workflow consists of a sequential staining strategy of ISH followed by IHC under basic (pH 9.0) HIER conditions with the ProK digestion (PIER) step at a low concentration (0.1 μg/mL). The optimized GeoMx SPG workflow requires a total of 4 days to complete from the slide preparation step to the data acquisition and analysis, which is described below. The GeoMx SPG workflow is compatible only with NGS readout including custom NGS probes and not compatible with nCounter readout (Fig. 1G).

The overall SPG workflow for FFPE samples is as follows:

i. **Day 1:** A two-step epitope retrieval process involving HIER under basic (pH 9.0) conditions followed by a PIER step using 0.1 μg/mL ProK. Samples are then incubated with the GeoMx WTA or GeoMx CTA RNA probe cocktails overnight for hybridization at 37°C.
ii. **Day 2:** Samples are washed under stringent conditions in the presence of 50% formamide and subsequently treated with a blocking solution to prevent nonspecific antibody binding. After blocking, samples are stained with one or more GeoMx NGS Protein panel(s) overnight at 4°C. Fluorophore-conjugated primary antibodies may be added at this step to visualize tissue morphology.
iii. **Day 3:** After fixing with 4% paraformaldehyde and staining with a nuclear marker (Syto13), samples are processed on the GeoMx DSP and

then sequenced on the Illumina NextSeq2000 or Illumina NovaSeq6000 as noted in Materials and Methods.

iv. **Day 4:** Process data with the GeoMx NGS Pipeline as described in Materials and Methods.

The GeoMx platform offers the researcher the ability to profile different sizes (minimum of 5 μm × 5 μm to maximum of 660 μm × 785 μm) and shapes (circular, rectangles, squares, polygons) of ROIs. The approximate number of cells captured by various ROI sizes have been determined and are follows: 50 μm (15 cells), 100–200 μm (100 cells), 250 μm (250 cells), 400 μm (480 cells; refs. 29, 31, 36). A maximum number of ROIs that can be placed on a single scan is 380.

The recommended ROI size for optimal detection of protein and RNA using the Proteogenomic GeoMx assay are as follows: nonsegmented geometric ROIs of 50–200 μm diameter circles and segmented ROIs of 50–300 μm diameter circles. It should be noted that smaller size ROIs (50 μm; ∼15 cells) will provide insight into medium- and high-expressing targets and subsequent pathway enrichment analysis. For the detection of low expressors and more robust analysis such as cell type deconvolution and DE analysis, ROIs > 100 μm (>50 and >100 cells for protein and RNA, respectively) are recommended.

Profiling of Cell Lines Using the Optimized GeoMx SPG Workflow

Using the optimized GeoMx SPG assay workflow, we profiled FFPE CPA sections using the GeoMx Human WTA and the 15-modular GeoMx Human NGS Protein panel simultaneously (147-plex; Supplementary Table S3). The GeoMx Human Protein Assays with NGS readout enables to profile of up to 144 protein targets (plus additional three IgG controls) simultaneously. As protein and RNA controls, CPAs were independently stained with the standard single-analyte GeoMx Human NGS Protein panel (147-plex) or with the standard single-analyte GeoMx Human WTA, respectively.

During the technical development of the SPG assay, we used a combination of 59-plex Human NGS protein panels (including IgG controls). Once the SPG assay was developed, we increased the number of panels to 15, composed of 147 proteins (147-plex, including IgG controls). By profiling FFPE samples of 45 different cell lines, the correlation of these two assays was tested. The SNRs of the SPG assay data using the 147-plex protein panel demonstrated a strong correlation ($R = 0.92$) between proteins that overlap with the original 59-plex protein panel (Fig. 2A). This finding suggests that more than doubling the number of proteins measured had little impact on assay performance.

Using the 147-plex Human NGS protein panel, we compared the performance of the SPG assay with the protein control assay. There was a strong correlation ($R = 0.92$) and the distribution of SNR counts were comparable between the two workflows (Fig. 2B; Supplementary Fig. S6A). Furthermore, both the single-analyte protein and SPG assay was reproducible across multiple users and instruments, where a very strong correlation ($R = 0.99$) was observed (Fig. 2C; Supplementary Fig. S6B). A pairwise correlation analysis was performed across 37 cell lines and all detectable targets (SNR ≥ 3). In the cell line to cell line comparison, the Pearson R was calculated between each cell line from the SPG assay against all cell lines in the single-analyte control. A dot plot was generated showing the Pearson R distribution for each cell line. There was a high correlation between the same cell lines in these two assays (Fig. 2D). In addition, we observed a high correlation between protein targets regardless of assay type in the target-to-target comparison across cell lines (Supplementary Fig. S7). To preserve the phosphorylation state of phosphorylated proteins, cell lines SKBR3, A431, and SH-SY5Y, making up the 45 CPAs, had been treated with a phosphatase inhibitor prior to paraformaldehyde fixation. The inhibitor treatment of cell lines partially drives a high correlation among phospho-specific antibodies as observed in the target-to-target heatmap (Supplementary Fig. S7).

For cellular activities, protein phosphorylation plays a critical role in the regulation of various cellular processes including cell signaling, gene expression, and cell growth and differentiation. Aberrant phosphorylation events are associated with several diseases including cancer, neurodegenerative disorders, and metabolic disorders. While transcriptomics enables the comprehensive profiling of cell and tissue specific gene expression, it is unable to decipher the phosphorylation state of key proteins. To study phosphorylation-related diseases and biological activities, using phospho-specific antibodies is one way to capture the phosphorylation state of the proteins. Approximately 12% of the antibody content in the proteomic portion of the SPG assay includes a number of phospho-epitope–specific antibodies, important for the exploration of signaling pathways (MAPK and PI3K) and neuropathology (hyperphosphorylated Tau). The performance of the phospho-specific protein detection from FFPE cell lines under SPG assay conditions was similar to the single-analyte protein control ($R = 0.91$; Fig. 2E; Supplementary Fig. S8). Furthermore, the performance of the phospho-specific detection with the SPG assay was reproducible across multiple users and instruments ($R = 0.99$; Fig. 2F; Supplementary Fig. S8).

We evaluated the change in sensitivity, as denoted by the average change in regression line slope, of the SPG assay compared with the single-analyte protein control (Fig. 2G). Using homogenous cell pellets minimized the confounding variables associated with section-to-section variability and precisely matching ROIs across multiple tissue samples. In our analysis, we observed an 11% decrease in sensitivity for the SPG assay.

In addition to evaluating the detection of protein targets, we examined the data quality of the RNA targets detected with the SPG assay in comparison with the RNA control and the CCLE RNA-seq dataset. A strong correlation ($R = 0.86$) was observed when comparing the single-analyte RNA control with the SPG assay (Fig. 2H). In the violin plots, a slight decrease in sensitivity was observed for the SPG assay (Supplementary Fig. S9A). As with the protein analyte, there was a high correlation ($R \geq 0.86$) between multiple users and instruments for both the SPG and the single-analyte RNA assay (Fig. 2I; Supplementary Fig. S9B). Furthermore, we observed a 15% decrease in sensitivity for SPG assay compared with the single-analyte control (Fig. 2G). For all overlapping targets between the GeoMx Human WTA and the CCLE RNA-seq dataset, each cell line in the proteogenomic assay and the RNA control were correlated to every cell line in the CCLE dataset (1,012 cell lines). For both the SPG and RNA control assays, we observed the highest correlation between matched cell lines to the CCLE RNA-seq dataset (Fig. 2J). The target-to-target comparison of single-analyte WTA control with SPG WTA data indicated a high correlation between RNA targets between assay types (Fig. 2K).

GeoMx SPG Assay in Human Tissue

Having validated the SPG assay on idealized cell pellet samples, we sought to evaluate the assay on human colorectal cancer samples. We profiled matched immune ($CD45^+$) and tumor ($PanCK^+$) regions in serial FFPE tissue sections stained with the GeoMx Human WTA and/or the 147-plex modular GeoMx

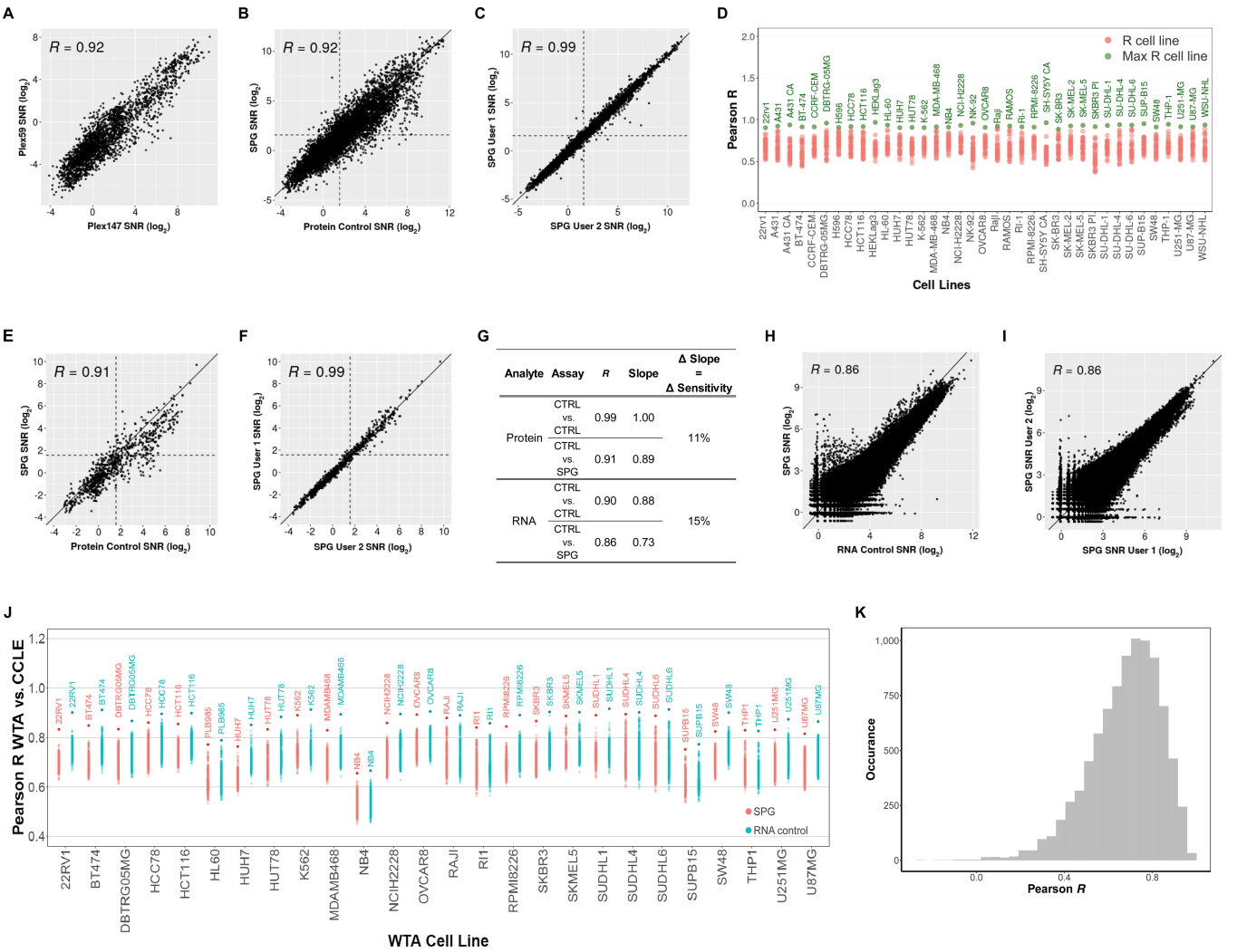

FIGURE 2 Assessment of SPG data quality versus the respective RNA and Protein control data. Assay correlation with respect to the protein analyte comparing 147-plex and 59-plex protein panel (**A**), protein control and proteogenomic workflows (**B**), and user-to-user and instrument-to-instrument reproducibility (**C**). **D,** Cell line to cell line comparison of protein control with proteogenomic protein data. For protein targets with SNR $\geq$ 3, the Pearson *R* was calculated between each cell line from the Protein Control slide against all the cell lines in the SPG slide. The max R cell line between the SPG and Protein control is labeled and highlighted green. Assay correlation of 17 phospho-specific antibodies between protein control and proteogenomic workflows (**E**) and user-to-user and instrument-to-instrument reproducibility (**F**). **G,** Assay correlation with respect to the RNA analyte comparing summary of Pearson R, the slope of linear regression, and change in sensitivity between workflows. The change in sensitivity corresponds to the average change in regression line slope between the SPG and the single-analyte control assay. RNA control and proteogenomic workflows (**H**) and user-to-user and instrument-to-instrument reproducibility (**I**). **J,** Cell line to cell line comparison of WTA control and proteogenomic WTA data to the entire CCLE RNA-seq dataset. For all overlapping targets between the CCLE and WTA data, the Pearson *R* in the protein control and SPG WTA data were calculated against all cell lines in the CCLE RNA-seq. Cell line labels in the plot correspond to SPG or GeoMx WTA cell lines with the highest R correlation to the CCLE data. **K,** Target-to-target comparison of WTA control to proteogenomic WTA data. For each RNA target with SNR $\geq$ 4, the Pearson *R* was calculated between WTA control $\log_2$ SNR transformed data and the respective proteogenomic WTA $\log_2$ SNR transformed data. Histogram shows the distribution of Pearson *R*.

Human NGS Protein panels. For these experiments, geometric ROIs (100 μm diameter circles) were collected for each morphology-specific regions (Fig. 3A; Supplementary Fig. S10A and S10B). In colorectal cancer samples, we observed a high correlation ($R \geq 0.80$) across ROIs between the SPG assay as compared with the single-analyte protein (Fig. 3B) and RNA assays (Fig. 3C). The correlations were higher in cell lines; however, this is to be expected given variables associated with section-to-section variability or precisely matching ROIs across multiple slides. We then performed a correlation analysis on all CD45-enriched or PanCK-enriched ROIs between the SPG assay and the single-analyte protein or RNA assays. Protein targets with SNR $\geq$ 3 and WTA RNA targets with SNR $\geq$ 4 were used in the analysis. A dot plot was generated showing the Pearson *R* distribution for each ROI. In this analysis, we observed a high correlation between immune ROIs and between tumor ROIs from the SPG and single-analyte controls (Supplementary Fig. S11A and S11B).

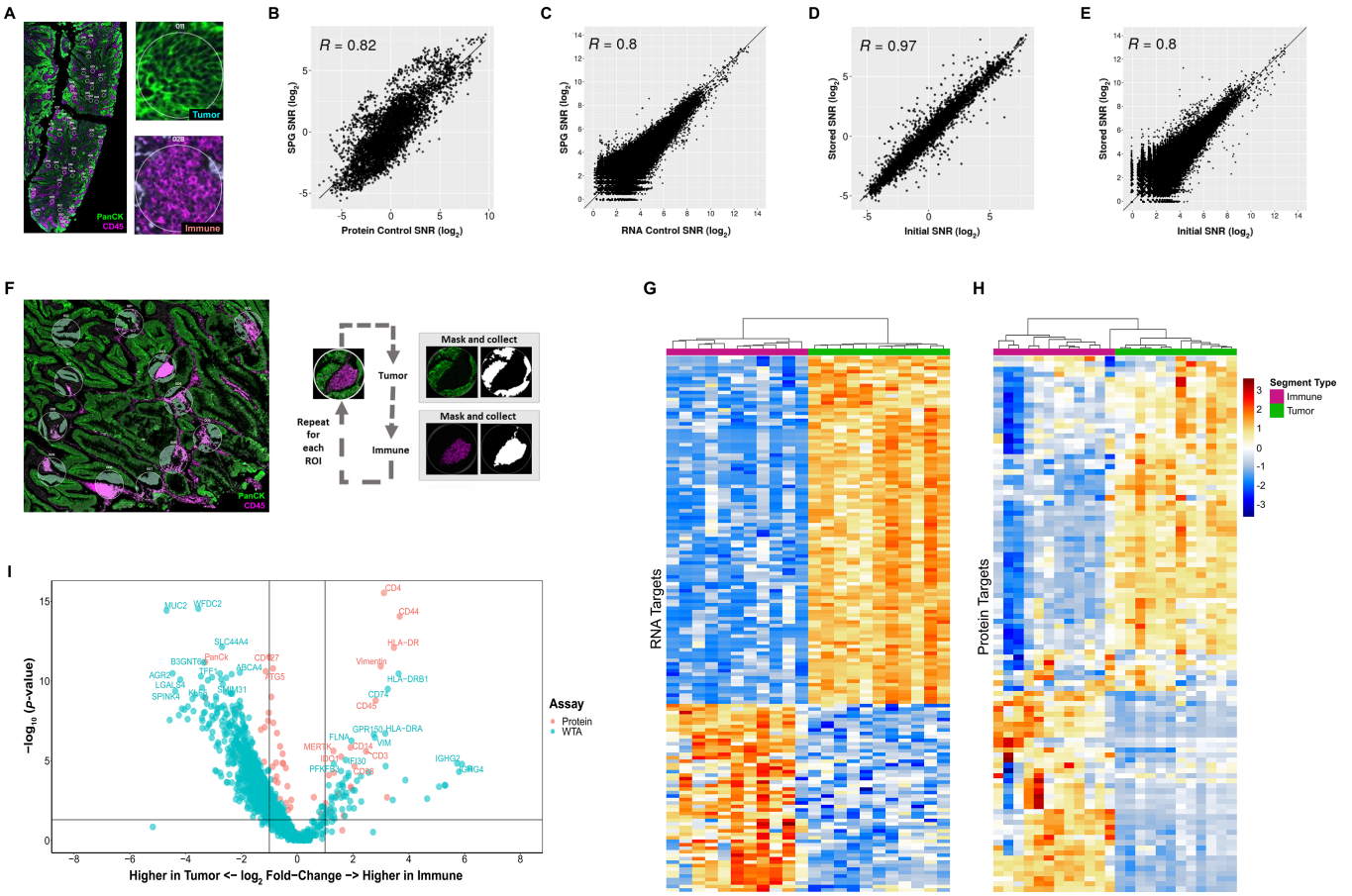

FIGURE 3 Assessment of SPG performance on human tissue. FFPE colorectal cancer sections were stained with the GeoMx NGS Human Protein modules (147-plex), WTA, and antibodies against PanCK (Tumor) and CD45 (Immune). **A,** Representative image of colorectal cancer sample used in the assessment of SPG data quality versus the respective RNA and Protein control data. Two ROIs showing strong enrichment of immune cells (CD45; magenta) and tumor cells (PanCK, green). Concordance between the proteogenomic assay and single analyte protein (**B**) and RNA controls (**C**). Concordance between the initial and stored proteogenomic slide for protein (**D**) and RNA analytes (**E**). **F,** Multiplexed protein and RNA characterization of colorectal cancer sample with representative images highlighting the segmentation of 300 μm circular ROIs into tumor- (PanCK$^+$) and immune- (CD45$^+$) enriched regions. Segments illuminated in white were collected, black regions were not. Protein targets with SNR ≥ 3 and WTA RNA targets with SNR ≥ 4 were used in the analysis. Unsupervised hierarchical clustering of top 250 differentially expressed RNA (**G**) and detect protein targets for colorectal cancer (**H**). **I,** Combined volcano plot of Protein and RNA expression in colorectal cancer. A subset of differentially expressed genes is labeled with colors matching their analyte.

We were also interested in the ability to profile colorectal cancer samples that had been stored in 1X TBS-T at 4°C, protected from light for 1-week post-initial DSP collection. One of the key benefits of using the GeoMx DSP platform for spatial profiling is that it entails a nondestructive process where tissue sections can be stored and reprofiled on additional ROIs (29). In this experiment, each sample slide contained two FFPE colorectal cancer tissue serial sections, one of which was used in the initial DSP profiling. We matched ROIs from the initial collection onto the unprofiled section without a stripping/reprobing process. As expected, profiling of the SPG assay slide post-1-week storage provided a high correlation to the initial profiling data for both the protein (R = 0.97) and RNA (R = 0.80) analytes (Fig. 3D and E). Together, we demonstrated high concordance between ROIs across serial sections and slides; more importantly, samples can be stored for additional DSP profiling runs.

Optical Segmentation with SPG Assay

We then explored the optical dissection capabilities of the GeoMx segmentation function using the SPG assay. The ability to optically dissect a tissue based on morphologic or biological features is an advantage for profiling protein and RNA targets in the distinct spatial context and within specific cell subpopulations. Using the segmentation strategies of the GeoMx DSP, we assessed the performance of the SPG assay on human colorectal cancer tissue samples. Applying the established SPG assay workflow, tissue sections were stained with the GeoMx Human WTA probe set and the 147-plex modular GeoMx Human NGS Protein panel, along with fluorescent dye–conjugated primary antibodies for CD45 and PanCK. Twelve circular ROIs of 300 μm in diameter were segmented into the AOIs of CD45-enriched immune and PanCK-enriched tumor cell subpopulations. The ROIs were selected across the various tumor regions within the tissue section, including tumor regions proximal to

immune-rich or immune-poor regions (Fig. 3F; Supplementary Fig. S10B). To analyze expression patterns within the segmented AOIs, we performed unsupervised hierarchical clustering of the top 250 differentially expressed RNA and detected protein (SNR $\geq$ 3) targets. As expected, we observed distinct clustering of targets within immune segments and tumor segments (Fig. 3G and H).

We performed DE analysis between CD45-enriched immune and PanCK-enriched tumor segments for both analytes. As shown in the volcano plot (Fig. 3I), we observed robust codetection of immune-related protein and RNA targets in the CD45-enriched segments whereas tumor-associated targets were observed in PanCK-enriched segments. In addition, an examination of expression levels of key RNA/Protein target pairs associated with either immune or tumor segments illustrates the variability of certain targets in a distinct immune or tumor AOI (Supplementary Fig. S12). For example, we observed high levels of HLA-DR protein/RNA target pair in immune segments and low in tumor. The opposite was true for cytokeratins, where high levels were observed in tumor segments and low levels in immune. Some RNA/protein target pairs, for example, RPS6, a critical component to translational activities, were expressed at high levels in all segments.

When considering the correlations of all detectable protein targets and RNA targets in either immune or tumor segmented AOIs, we noted distinct patterns of positive and negative correlation. For example, IFNγ-inducible protein 30 (IFI30) is expressed in most antigen-presenting cells (APC), including monocytes, macrophages, and dendritic cells, where it functions in MHC class II-restricted antigen processing and has been shown to have a role in the immune response to malignant tumors such as melanoma, prostate cancer, and glioma (37–40). In the immune AOIs, there was a strong positive correlation between the *IFI30* gene and protein targets associated with MHC class II presentation on macrophages (CD68, CD14, HLA-DR), Th cells (CD4, CD127), dendritic cells (S100B) and tumor cells or activated APCs (B7-H3; Supplementary Fig. S13). On the contrary, we observed a negative correlation of the *IFI30* gene with CD20 (B cells) and CD95/Fas (cell death) and CD8 (cytotoxic T cells; Supplementary Fig. S13). In the tumor segments, a negative correlation between the *MUC5AC* RNA target associated with mucus production in goblet cells and the protein target PanCK (tumor cell marker) was observed (ref. 41; Supplementary Fig. S14). Conversely, there was a positive correlation between the *MUC5AC* RNA target and autophagy-related protein targets ATG5, ATG12, LAMP2A, and BAG3. Normal regulation of mucus production commonly involves autophagy for the regulation and secretion of mucins (42, 43). Abnormal expression of MUC5AC is commonly associated with malignant colorectal cancerous cells (41), as observed in our data (Supplementary Fig. S14).

In addition to colorectal cancer tissues, we also evaluated the GeoMx segmentation capabilities on human NSCLC samples. Tissue sections were stained with the GeoMx Human WTA and the 147-plex modular GeoMx Human NGS Protein panel, along with primary antibodies for CD45 and PanCK for visualization. Twelve circular ROIs of 300 μm in diameter were selected across various tumor regions and segmented into CD45-enriched immune and PanCK-enriched tumor subpopulations (Supplementary Fig. S15A). As with colorectal cancer, the DE analysis demonstrated robust codetection and specificity of both protein and RNA targets within each segment type (Supplementary Fig. S15B). Furthermore, we observed distinct clustering of RNA and protein targets within immune segments and tumor segments (Supplementary Fig. S15C).

Performance of SPG Assay on Mouse Tissue

Given the frequent use of mouse models for studying various human biology and diseases, we examined our SPG assay on mouse tissue samples. For profiling, FFPE mouse multiorgan TMA sections were stained with the GeoMx Mouse WTA (21,000+ protein-coding genes) and the 15-modular GeoMx Mouse NGS Protein panel (137-plex; Supplementary Table S4). In parallel, TMAs were stained with the standard single-analyte 137-plex GeoMx Mouse NGS Protein panel or with the standard single-analyte GeoMx Mouse WTA, used as the protein and RNA controls, respectively. For these experiments, circular ROIs (100 μm diameter) were selected for multiple tissue types including thymus, small intestine, kidney, and seminal vesicle (Fig. 4A, middle; Supplementary Fig. S16). In each tissue type, there was a strong correlation between the single-analyte RNA data and the SPG assay data on the small intestine ($R = 0.82$), thymus ($R = 0.70$), kidney ($R = 0.76$), and seminal vesicle ($R = 0.71$; Fig. 4A, top). Like that of human colorectal cancer tissue samples, the correlations were higher in cell lines; however, this is to be expected given variables associated with section-to-section variability or precisely matching ROIs across multiple slides. When we performed unsupervised hierarchical clustering on matched AOIs between the SPG assay and single-analyte RNA data, there was a high concordance between matched ROIs as well as a high correlation between tissue-specific ROIs (Supplementary Fig. S17A). In the unsupervised hierarchical clustering analysis of the top 400 detected RNA targets, we observed distinct clustering with respect to tissue type (Fig. 4B).

For protein profiling, the correlation between the SPG assay data to the single-analyte protein data was strong ($R \geq 0.97$) for all mouse tissue types tested (Fig. 4A, bottom). In an unsupervised hierarchical clustering on matched ROIs between the SPG assay and single-analyte protein data in each tissue type, there was a high concordance between matched ROIs as well as a high correlation between tissue-specific ROIs (Supplementary Fig. S17B). Furthermore, we observed distinct clustering of protein targets within specific tissue types (Fig. 4C). When we examined the expression level of several RNA/protein target pairs, there was a high concordance between the two analytes for GAPDH, S6, Histone H3, whereas a subset of targets was detectable only at the protein level (B7-H3, CD34, CD68, GZMB, S100B; Supplementary Fig. S18).

Glioblastoma Study Using SPG Assay

After successfully developing a SPG assay and evaluating its performance on various cell lines and tissues, we assessed the performance of the SPG assay in another biological context using a brain glioblastoma tissue array. GBM is a highly aggressive, grade IV astrocytoma that accounts for 49% of all primary malignant brain tumors (44, 45). Despite low incidence compared with other human cancers, glioblastomas are considered one of the deadliest (45, 46). The low numbers of patients coupled with high intratumor and intertumor heterogeneity have presented an obstacle to developing glioblastoma treatments or providing formal subtypes that could contribute to therapeutic understanding (47). Initially, even cytologic or IHC characteristics were difficult to solidify (48). The advancement of technology, however, has expanded knowledge of the molecular and genetic hallmarks of glioblastoma subtypes. The cytological hallmark of any GBM subtypes is the result of several mutations acting in concert. In addition, overactivity of both PI3K/AKT and MAPK/ERK pathways drives cell proliferation and differentiation, a characteristic of GBM (49). It is also clear that these features have a variety of effects on prognosis (50, 51).

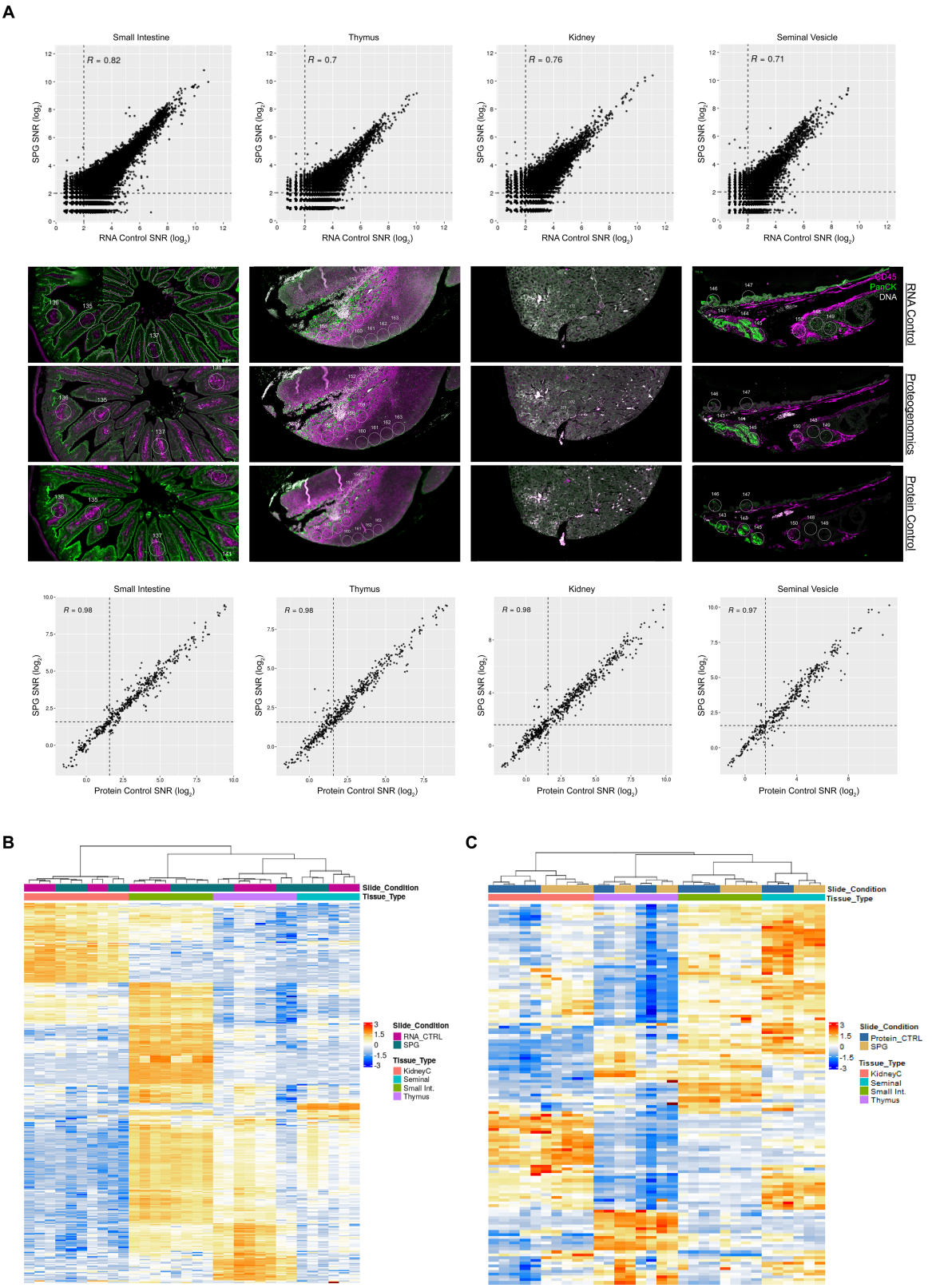

FIGURE 4 Spatial proteogenomics across mouse tissue types. High-plex SPG characterization of mouse tissues with matched circular ROIs. FFPE sections were stained with GeoMx Mouse WTA (RNA control), 15-stacked GeoMx Mouse Protein Modules (137-plex; protein control), or both analytes simultaneously with the SPG workflow. **A,** Concordance and representative images of mouse tissue used in the assessment of the SPG versus the respective RNA (top) and protein (bottom) control. Unsupervised hierarchical clustering of top 400 expressing RNA targets with an SNR $\geq$ 4 (**B**) and detected protein targets (SNR $\geq$ 3; **C**) across all tissue types.

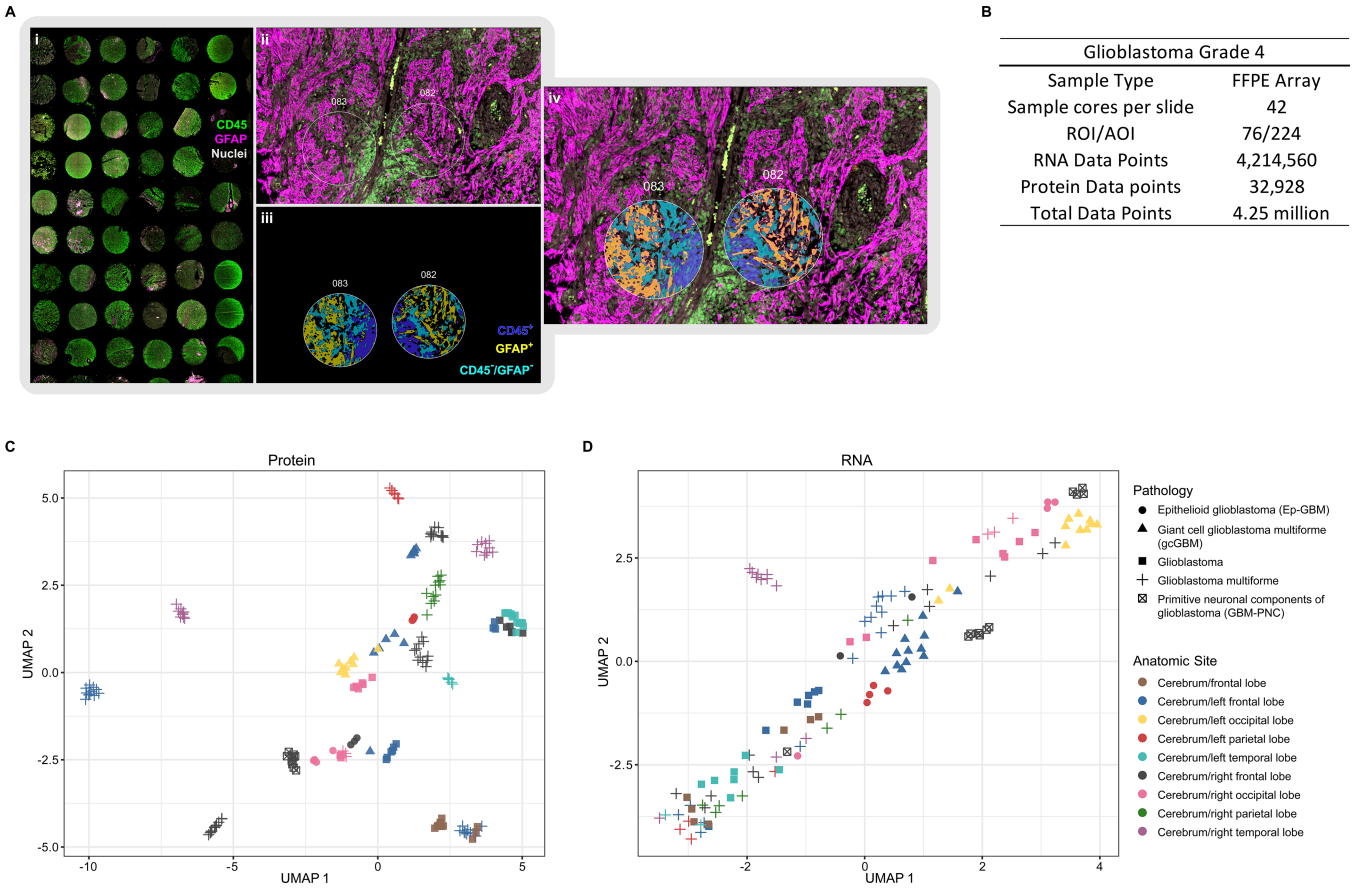

B

Glioblastoma Grade 4	
Sample Type	FFPE Array
Sample cores per slide	42
ROI/AOI	76/224
RNA Data Points	4,214,560
Protein Data points	32,928
Total Data Points	4.25 million

FIGURE 5 SPG exploration of GBM grade 4. **A,** A total of 42 cores across 23 distinct sample sources and multiple GBM types. ROIs were segmented into CD45$^+$, GFAP$^+$, or CD45$^-$/GFAP$^-$. **B,** Statistics from a single slide and single GeoMx SPG run. UMAP plots for protein (**C**) and RNA analytes (**D**).

Giant cell glioblastoma multiforme (gcGBM) are of particular interest, as they are consistently associated with complete resection and improved survival (52). As another hallmark of gcGBM, giant, multinucleated cells have been linked to distinct, dysfunctional aspects of DNA damage signaling (53) and cell-cycle checkpoints (54). Though many promising molecular targets for therapy have been identified (37–41), a better understanding of the tumor microenvironment and the tumor heterogeneity is needed for the development of more effective and targeted therapies (55–59).

A SPG approach offers a robust way to identify impactful interactions between analytes. In this study, we profiled 23 different cases across four different pathologic (grade 4) subtypes including GBM (17 cases), epithelioid glioblastoma (Ep-GBM; three cases), gcGBM (two cases), and primitive neuronal components of glioblastoma (PNC-GBM; one case). The TMA was stained with the GeoMx Human WTA and the 147-plex modular GeoMx Human NGS Protein panel along with fluorophore-conjugated primary antibodies for CD45 and GFAP to guide ROI selection and segmentation. A total of 76 circular ROIs, 300 μm in diameter, were segmented into CD45$^+$ (Immune), GFAP$^+$ (Astrocyte/Tumor), or CD45$^-$/GFAP$^-$ (Fig. 5A; Supplementary Fig. S19). GBM is a highly heterogeneous and disorganized tumor, where more advanced tumor types are more disorganized. The heterogeneous and disorganized nature of GBM makes it difficult to select clear tumor- and/or immune-enriched ROIs compared with colorectal cancer or NSCLC samples. Even in these highly disorganized samples, the segmentation capabilities of the GeoMx DSP allowed us to optically dissect immune and astrocytic/tumor cells (Fig. 5A; Supplementary Fig. S19 and S20). In total, 224 AOIs were collected; the resulting dataset was composed of 4.25 million data points (Fig. 5B).

In a UMAP dimension reduction analysis of GBM samples, we observed distinct clustering based on pathology and tumor anatomic location for both protein (Fig. 5C) and RNA (Fig. 5D). These findings suggest that the anatomic location and subtype of GBM contribute to overall pathology and the presence of molecular signatures. In a DE analysis between GFAP$^+$ (Astrocyte/Tumor) and CD45$^+$ (immune) segments using a cutoff of FDR $<$ 0.001 and fold change (FC) $>$2, we identified 25 proteins and 88 genes that were differentially expressed in a subset of samples.

The volcano plot highlights the DE of key targets for both protein and RNA (Fig. 6A). For example, in CD45-enriched segments, we noted the higher expression of key protein targets associated with immune response such as T-cell (CD4), macrophage/monocytes (CD68, CD163, CD14, CD11c), and dendritic cells (CD11c). In GFAP-enriched segments, tumor-associated proteins, such as CD56, CD44, and Tau (including phosphorylated variants S199, T231, and S404) were highly expressed (Fig. 6A; refs. 60–62). Similarly, we observed higher levels of mRNA transcripts associated with immune response, such as macrophages (*SRGN*, *C1QA*, *C1QB*, *C1QC*, *IFI30*) and neutrophils (*LCP1*, *LAPTM5*), in CD45-enriched segments, whereas GBM-associated genes such as *GFAP*, *DDR1*, *CRYAB*, *SOX2*, *TTYH1* were expressed higher in GFAP-enriched segments (Fig. 6A; refs. 62–69). Unsupervised

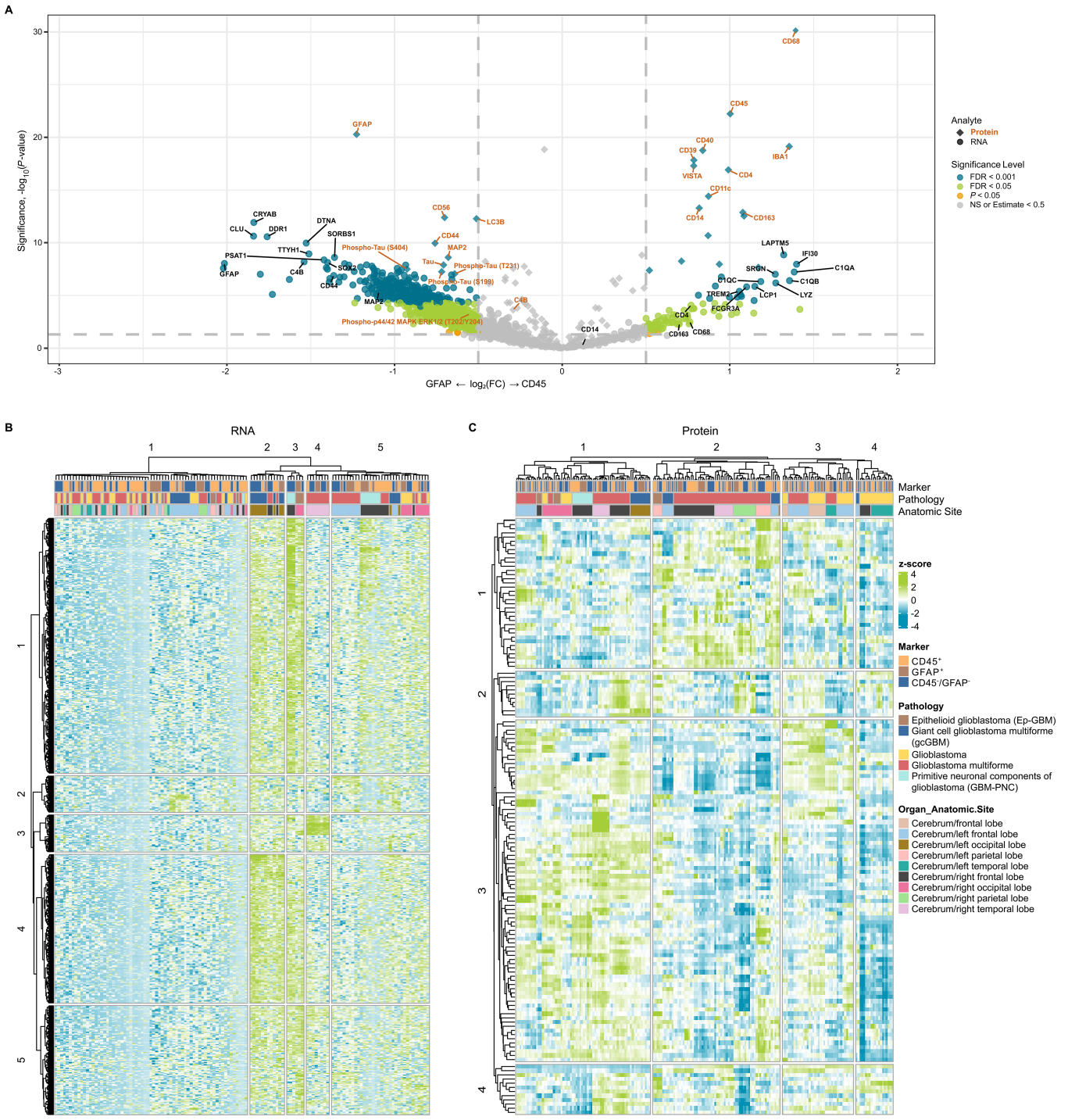

FIGURE 6 DE analysis between GFAP- and CD45-enriched segments. **A,** Combined volcano plot resulting from the DE analysis between GFAP- and CD45-enriched segments for RNA (●) and protein (♦) analytes. Targets with significant DE are highlighted either orange ($P < 0.05$), green (FDR < 0.05) or blue (FDR < 0.001); whereas targets in gray show no significant difference in expression. A subset of differentially expressed targets is labeled. Unsupervised hierarchical clustering analysis of detected RNA (**B**) and protein (**C**).

hierarchical clustering analysis revealed distinct clustering of RNA (Fig. 6B) and protein (Fig. 6C) targets with respect to pathology as well as anatomic location. These observations are consistent with the UMAP analysis, showing that the anatomic location of tumors contributes to the molecular signatures of GBM subtypes.

As noted above, GBM can be classified into several subtypes, one of which is gcGBM. In this study, one of our interests was identifying transcriptomic and proteomic signatures that differentiate gcGBM from GBM. To mitigate the influence of the tumor anatomic location on these different pathologies, we focused our analysis on left frontal lobe tumors, as a result, the analysis was based

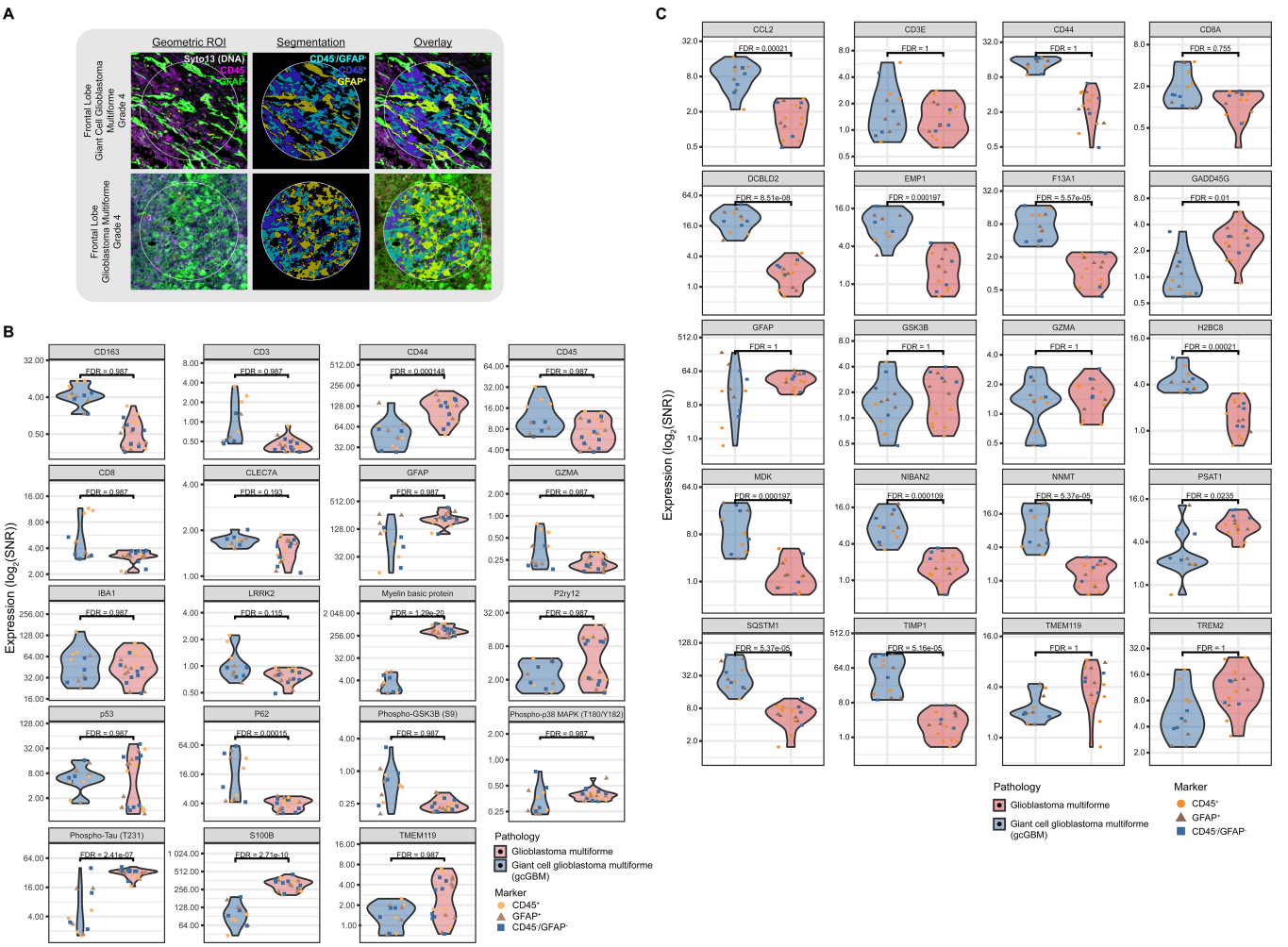

FIGURE 7 SPG exploration of gcGBM and GBM. **A,** Representative images of ROIs segmented into CD45$^+$, GFAP$^+$, or CD45$^-$/GFAP$^-$. Top differentially expressed protein targets (**B**) and RNA targets (**C**) from frontal lobe gcGBM as compared with GBM, all grade 4.

on a limited number of patient cases, one gcGBM and two GBM samples. Each case contained two tissue cores and two ROIs per core which were segmented into three AOIs: CD45$^+$, GFAP$^+$, or CD45$^-$/GFAP$^-$ (Fig. 7). In a DE analysis (FDR $<$ 0.001, FC $>$ 2) on detected targets for each AOI within the left frontal lobe, we identified a total of 19 and four differentially expressed genes and proteins, respectively between the two pathologies (Supplementary Fig. S21). For protein data, we also performed a DE analysis between GBM and gcGBM for CD45- (Supplementary Fig. S22A) or GFAP- (Supplementary Fig. S22B) enriched segments. Using a cutoff of $P < 0.05$, FDR < 0.001, and FC > 2, we identified a total of 14 and seven differentially expressed proteins in CD45- and GFAP-enriched segments, respectively.

While the limited number of patient cases used in our analysis is insufficient for the complete elucidation of subtype-specific molecular signatures, we did observe several genes and proteins in gcGBM with distinct expression profiles compared with GBM (Fig. 7; Supplementary Fig. S21 and S22). For example, we observed DE of protein targets, CD3 and CD8, associated with infiltrating total T cells and CTLs, respectively (Fig. 7B; Supplementary Fig. S22A). Immune infiltration has been noted as a characteristic of gcGBM (57, 70, 71). As the prognostic role of CD3 and CD8 has yet to be established in gcGBM, there are numerous reports associating infiltrating lymphocytes with improved prognosis for several cancers (72–75). In our analysis, both CD3 and CD8 proteins were expressed at least 2-fold higher in several CD45-enriched AOIs of gcGBM compared with the same type of AOI in GBM samples (Fig. 7B). At the transcript level, *CD3E* and *CD8A* did not appear to be significantly differentially expressed between the two pathologies (Fig. 7C; Supplementary Fig. S21).

We also evaluated several targets associated with tumor proliferation and/or migration to discriminate gcGBM from GBM. *GFAP*, for example, shows differential RNA expression with a lower average (and wider range) of SNR in gcGBM than GBM samples (Fig. 7C). This difference in expression between the two pathologies is maintained in GFAP protein (Fig. 7B), which is known to positively correlate with advancing neuroglial tumor grade (76).

Enrichment of S100B has been shown to be sufficient to drive angiogenesis, increase tumor inflammation (77), enhance growth (78), and drive migration (79), all of which are features of GBM. The proposed tumorigenic contribution of S100B has been associated with its ability to attenuate the tumor-suppressive activity of p53 by inhibiting p53 phosphorylation and regulating cell proliferation and differentiation through increasing mitogenic kinase Ndr (80) and Akt (81) activity (78). *In vitro* studies involving cell lines derived from

malignant glioblastoma shown that the attenuation of S100B expression decreased the number of invading cells whereas upregulation resulted in an increase in invading cells (82). In our analysis, S100B protein expression in gcGBM was decreased at least 2-fold in all AOI as compared with GBM (Fig. 7B; Supplementary Fig. S22). While it has been reported that higher expression levels of S100B in patients with GBM are associated with shorter overall survival (82), it is unclear what role S100B may play in the favorable prognosis of gcGBM compared with GBM.

While CD44, at the protein level, exhibited a broad range of expression for both pathologies, the average expression level of RNA was at least 2-fold higher in gcGBM than that of GBM (Fig. 7B and C). CD44 expression is critical for GBM invasion and migration; more importantly, GBM cells with higher levels of CD44 have been associated with poor prognosis (60, 61, 83, 84).

In our analysis, the average expression level for Myelin basic protein (MBP) in gcGBM was at least 64 times lower in all AOIs compared with GBM samples (Fig. 7B; Supplementary Fig. S22). On the other hand, DE at the transcript level was not observed. MBP has been viewed as a potential biomarker for various types of tumors including glioblastoma in cerebrospinal fluids (85–87). In other studies, MBP was highly expressed in oligodendroglioma while minimally expressed in GBM (88). It has been suggested that MBP may play a role in the progression and potential treatment of multiple sclerosis; however, it is unclear what role it has in gcGBM biology (89).

As noted earlier, the phosphorylation state of proteins can only be captured through protein and not transcriptomic analysis. GSK3β is part of the PI3K-AKT/mTOR pathway whose phosphorylation state plays an important role in glycogen synthesis, apoptosis, angiogenesis, and cell cycle. In our dataset, protein expression levels of phospho-GSK3β (Ser9) were broad and at least 2-fold higher for several AOIs in the gcGBM sample compared with GBM sample AOIs (Fig. 7B). Phosphorylation at Ser9 of GSK3β leads to its inactivation, which in turn prevents the phosphorylation and subsequent degradation of β-catenin. Active β-catenin has been shown to drive cell proliferation in GBM (90–92). We also observed differential protein expression phosphorylated Tau variants. Phospho-Thr231 Tau was at least 2-fold higher for several AOIs in the GBM sample compared with gcGBM (Fig. 7B; Supplementary Fig. S22). Whereas Tau, pSer199 Tau, and pSer404 Tau were only expressed at higher levels in GBM than gcGBM within the GFAP-enriched AOIs (Supplementary Fig. S22B). While associated with neurodegenerative diseases such as Alzheimer's disease, altered Tau expression has been observed in several cancers including glioblastoma (93–98). Like with the other targets mentioned above, based on our limited dataset, it is not clear what role these phosphorylated proteins play in GBM cell migration, survival, and apoptosis. Though limited in size, our study exemplifies the utility of the SPG assay and its potential contribution to expanding our understanding of GBM molecular pathology.

Discussion

To better understand the relationship between RNA and protein within a spatially defined cell population, we have developed a high-plex, GeoMx DSP SPG assay with NGS readout to simultaneously detect RNA (whole transcriptome, >18,000-plex) and protein (>100-plex) from a single tissue section slide. We have confirmed that the sensitivity and specificity for both analytes under SPG assay conditions are comparable with single-analyte conditions where only a slight loss of sensitivity (<15%) is observed for both analytes. The slight loss in sensitivity is a tradeoff when implanting the SPG assay given that the two analytes required two distinct and disparate antigen retrieval conditions for optimal detection. We have highlighted several use cases in cell lines and tissue derived from human and mouse to demonstrate how this workflow can be leveraged to accurately measure RNA and protein within the same sample. In addition, we demonstrate simultaneous high-plex detection of distinct immune or tumor RNA and protein targets from spatially resolved individual cell subpopulations in human colorectal cancer, NSCLC, and GBM using the tissue segmentation capabilities of the GeoMx DSP with the SPG assay. Unlike colorectal cancer and NSCLC, GBM is a highly heterogeneous and disorganized tumor, where selecting the clearly defined immune- and/or tumor-enrich regions can be challenging. However, using the GeoMx DSP, we were able to optically dissect immune and astrocytic/tumor cells in various GBM subtypes. While the GBM study was restricted in scope due to the limited number of case samples, we did observe distinct clustering of both RNA and protein data based on pathology and anatomic location. Furthermore, we were able to identify the DE between GBM and gcGBM for several protein and RNA targets.

Overall, the SPG assay expands upon the capabilities of the GeoMx DSP and enables researchers to conduct a comprehensive molecular analysis while preserving precious samples. Profiling RNA or protein alone will only provide a limited picture of the biological system under study, especially when the correlation between RNA expression and protein abundance can be poor, as highlighted in several of our use case studies (2–5). We also identified several targets that could only be detected by protein and not by RNA. One of the key advantages of implementing the SPG assay is that it enables the profiling of both RNA and protein from identical cell populations while eliminating the technical variation (i.e., section-to-section variation and precisely matching ROIs across multiple samples) introduced when performing single-analyte assays. More importantly, the SPG assay provides an efficient means of profiling two analytes from a single slide as opposed to running two separate slides, one for each analyte.

Another advantage of the SPG workflow, as with all GeoMx assays, is that the process is nondestructive which allows the researcher to store and reprofile their samples. Furthermore, it uses modular GeoMx reagent panels that are validated for use in high-plex studies and can be customized with additional targets. More importantly, GeoMx Protein reagents contain antibodies specific to intracellular and phosphorylated protein targets. The detection and quantification of phosphorylated proteins can only be achieved at the protein and not RNA level by using phospho-specific antibodies. We have shown that the GeoMx SPG assay in FFPE tissues across species gives comparable specificity to the single-analyte GeoMx assays, with only a minor decrease in overall sensitivities, demonstrating a high-quality multimodal omic workflow compatible with the GeoMx DSP platform.

Transcriptomics and proteomics work in concert to describe cell activity, cell function, and cell-to-cell communication. Profiling RNA expression gives insight into the cellular blueprints and assessing proteins describes the cellular architecture, functions, and cell-to-cell communications. But each in isolation is only part of the necessary whole. The ability to profile both RNA and protein analytes simultaneously, at ultra high-plex within a spatially resolved single population of cell types, helps to close the knowledge gap between these two omics, paving the way for critical SPG investigations and discoveries within the rapidly emerging field of spatial biology.

Authors' Disclosures

A.B. Rosenbloom is a current employee of NanoString Technologies and holds NanoString stock or stock options. G.T. Ong reports other from NanoString Technologies during the conduct of the study; other from NanoString Technologies outside the submitted work. D. Newhouse reports other from NanoString outside the submitted work. F. New reports personal fees from NanoString Technologies outside the submitted work. H. Sato reports other from NanoString Technologies during the conduct of the study. G. Geiss reports personal fees from NanoString Technologies during the conduct of the study; personal fees from NanoString Technologies outside the submitted work. J.M. Beechem reports other from NanoString during the conduct of the study. No disclosures were reported by the other authors.

Authors' Contributions

S.A. Bonnett: Conceptualization, data curation, software, formal analysis, validation, investigation, visualization, methodology, writing-original draft, writing-review and editing. **A.B. Rosenbloom:** Conceptualization, supervision, visualization, methodology, writing-original draft, project administration, writing-review and editing. **G.T. Ong:** Data curation, formal analysis, visualization. **M. Conner:** Formal analysis, validation, investigation, visualization. **A.B.E. Rininger:** Formal analysis, validation, investigation, visualization. **D. Newhouse:** Software, formal analysis, visualization. **F. New:** Software, formal analysis, visualization. **C.Q. Phan:** Validation, investigation. **S. Ilcisin:** Validation, investigation. **H. Sato:** Writing-review and editing. **J.S. Lyssand:** Resources. **G. Geiss:** Conceptualization, resources, supervision, project administration, writing-review and editing. **J.M. Beechem:** Resources, supervision, funding acquisition, writing-review and editing.

Acknowledgments

We thank Bridget Kulasekara, Karen Nguyen, Daniel R. Zollinger, Michelle Kriner, Michael Rhodes, Erin Piazza, and Margaret Hoang from NanoString Technologies for their insight and guidance. We also want to thank Corey Williams from NanoString for their help with NGS.

Note

Supplementary data for this article are available at Cancer Research Communications Online (https://aacrjournals.org/cancerrescommun/).

Received October 06, 2022; revised January 20, 2023; accepted April 04, 2023; published first May 03, 2023.

References

1. Hickey JW, Neumann EK, Radtke AJ, Camarillo JM, Beuschel RT, Albanese A, et al. Spatial mapping of protein composition and tissue organization: a primer for multiplexed antibody-based imaging. Nat Methods 2022;19: 284-95.
2. Nusinow DP, Szpyt J, Ghandi M, Rose CM, McDonald ER, Kalocsay M, et al. Quantitative proteomics of the cancer cell line encyclopedia. Cell 2020;180: 387-402.
3. Vogel C, Marcotte EM. Insights into the regulation of protein abundance from proteomic and transcriptomic analyses. Nat Rev Genet 2012;13: 227-32.
4. Edfors F, Danielsson F, Hallström BM, Käll L, Lundberg E, Pontén F, et al. Gene-specific correlation of RNA and protein levels in human cells and tissues. Mol Syst Biol 2016;12: 883.
5. Liu Y, Beyer A, Aebersold R. On the dependency of cellular protein levels on mRNA abundance. Cell 2016;165: 535-50.
6. Li DK, Wang W. Characteristics and clinical trial results of agonistic anti-CD40 antibodies in the treatment of malignancies (Review). Oncol Lett 2020;20: 176.
7. Ramiro L, García-Berrocoso T, Briansó F, Goicoechea L, Simats A, Llombart V, et al. Integrative multi-omics analysis to characterize human brain ischemia. Mol Neurobiol 2021;58: 4107-21.
8. Hasin Y, Seldin M, Lusis A. Multi-omics approaches to disease. Genome Biol 2017;18: 83.
9. Subramanian I, Verma S, Kumar S, Jere A, Anamika K. Multi-omics data integration, interpretation, and its application. Bioinform Biol Insights 2020;14: 1177932219899051.
10. Method of the year 2019: single-cell multimodal omics. Nat Methods 2020;17: 1.
11. Kochan J, Wawro M, Kasza A. Simultaneous detection of mRNA and protein in single cells using immunofluorescence-combined single-molecule RNA FISH. Biotechniques 2015;59: 209-21.
12. Guilliams M, Bonnardel J, Haest B, Vanderborght B, Wagner C, Remmerie A, et al. Spatial proteogenomics reveals distinct and evolutionarily conserved hepatic macrophage niches. Cell 2022;185: 379-96.
13. Ben-Chetrit N, Niu X, Swett AD, Sotelo J, Jiao MS, Stewart CM, et al. Integration of whole transcriptome spatial profiling with protein markers. Nat Biotechnol 2023 [Online ahead of print].
14. Demaree B, Delley CL, Vasudevan HN, Peretz CAC, Ruff D, Smith CC, et al. Joint profiling of DNA and proteins in single cells to dissect genotype-phenotype associations in leukemia. Nat Commun 2021;12: 1583.
15. Triana S, Vonficht D, Jopp-Saile L, Raffel S, Lutz R, Leonce D, et al. Single-cell proteo-genomic reference maps of the hematopoietic system enable the purification and massive profiling of precisely defined cell states. Nat Immunol 2021;22: 1577-89.
16. Dillon LW, Ghannam J, Nosiri C, Gui G, Goswami M, Calvo KR, et al. Personalized single-cell proteogenomics to distinguish acute myeloid leukemia from non-malignant clonal hematopoiesis. Blood Cancer Discov 2021;2: 319-25.
17. Kim Y, Danaher P, Cimino PJ, Hurth K, Warren S, Glod J, et al. Highly multiplexed spatially resolved proteomic and transcriptional profiling of the glioblastoma microenvironment using archived formalin-fixed paraffin-embedded specimens. Mod Pathol 2023;36: 100034.
18. Schulz D, Zanotelli VRT, Fischer JR, Schapiro D, Engler S, Lun XK, et al. Simultaneous multiplexed imaging of mRNA and proteins with subcellular resolution in breast cancer tissue samples by mass cytometry. Cell Syst 2018;6: 25-36.
19. Dikshit A, Zong H, Anderson C, Zhang B, Ma X-J. Simultaneous visualization of RNA and protein expression in tissue using a combined RNAscope™ *in situ* hybridization and immunofluorescence protocol. In: BS Nielsen, J Jones, editors. In situ hybridization protocols. New York (NY): Springer US; 2020. p. 301-12.
20. Grabinski TM, Kneynsberg A, Manfredsson FP, Kanaan NM. A method for combining rnascope *in situ* hybridization with immunohistochemistry in thick free-floating brain sections and primary neuronal cultures. PLoS One 2015;10: e0120120.
21. Ko JN, Jung JK, Park YI, Shin HJ, Huh J, Back S, et al. Multistaining optimization for Epstein-Barr virus-encoded RNA *in situ* hybridization and immunohistochemistry of formalin-fixed paraffin-embedded tissues using an automated immunostainer. J Pathol Transl Med 2019;53: 317-26.
22. Ikeda S. Novel and simple method of double-detection using fluorescence *in situ* hybridization and fluorescence immunostaining of formalin-fixed paraffin-embedded tissue sections. Oncol Lett 2018;15: 1084-8.

23. Chan S, de L'Etang AF, Rangell L, Caplazi P, Lowe JB, Romeo V. A method for manual and automated multiplex RNAscope in situ hybridization and immunocytochemistry on cytospin samples. PLoS One 2018;13: e0207619.
24. Officer LK, Andreou KE, Teodósio TA, He Z, le Quesne JP. Automated co-*in situ* hybridization and immunofluorescence using archival tumor tissue. In: BS Nielsen, J Jones, editors. In situ hybridization protocols. New York (NY): Springer US; 2020. p. 245-56.
25. Millar M. Mixed multiplex staining: automated RNAscope™ and OPAL™ for multiple targets. In: BS Nielsen, J Jones, editors. In situ hybridization protocols. New York (NY): Springer US; 2020. p. 277-98.
26. Roberts K, Bayraktar OA. Automation of multiplexed RNAscope single-molecule fluorescent *in situ* hybridization and immunohistochemistry for spatial tissue mapping. In: BS Nielsen, J Jones, editors. In situ hybridization protocols. New York (NY): Springer US; 2020. p. 229-44.
27. Rajthala S, Dongre H, Parajuli H, Min A, Nginamau ES, Kvalheim A, et al. Combined *in situ* hybridization and immunohistochemistry on archival tissues reveals stromal microRNA-204 as prognostic biomarker for oral squamous cell carcinoma. Cancers 2021;13: 1307.
28. Zollinger DR, Lingle SE, Sorg K, Beechem JM, Merritt CR. GeoMx™ RNA assay: high multiplex, digital, spatial analysis of RNA in FFPE tissue. Methods Mol Biol 2020;2148: 331-45.
29. Merritt CR, Ong GT, Church SE, Barker K, Danaher P, Geiss G, et al. Multiplex digital spatial profiling of proteins and RNA in fixed tissue. Nat Biotechnol 2020;38: 586-99.
30. Gupta S, Zugazagoitia J, Martinez-Morilla S, Fuhrman K, Rimm DL. Digital quantitative assessment of PD-L1 using digital spatial profiling. Lab Invest 2020;100: 1311-7.
31. Zimmerman SM, Fropf R, Kulasekara BR, Griswold M, Appelbe O, Bahrami A, et al. Spatially resolved whole transcriptome profiling in human and mouse tissue using digital spatial profiling. Genome Res 2022;32: 1892-905.
32. Bergholtz H, Carter J, Cesano A, Cheang M, Church S, Divakar P, et al. Best practices for spatial profiling for breast cancer research with the GeoMx® digital spatial profiler. Cancers 2021;13: 4456.
33. Gu Z, Eils R, Schlesner M. Complex heatmaps reveal patterns and correlations in multidimensional genomic data. Bioinformatics 2016;32: 2847-9.
34. Caruccio L, Byrne K, Procter J, Stroncek D. A novel method using formamide for the elution of antibodies from erythrocytes. Vox Sang 2002;83: 63-9.
35. Ghandi M, Huang FW, Jané-Valbuena J, Kryukov GV, Lo CC, McDonald ER, et al. Next-generation characterization of the cancer cell line encyclopedia. Nature 2019;569: 503-8.
36. Fropf R, Griswold M, Zimmerman S, Nguyen K, Reeves J, Fuhrman K, et al. The GeoMx® human whole transcriptome atlas for the digital spatial profiler: design, performance, and experimental guidelines. Available from: https://nanostring.com/resources/the-geomx-whole-transcriptome-atlas-for-the-digital-spatial-profiler-design-performance-and-experimental-guidelines/.
37. West LC, Cresswell P. Expanding roles for GILT in immunity. Curr Opin Immunol 2013;25: 103-8.
38. Zhu C, Chen X, Guan G, Zou C, Guo Q, Cheng P, et al. IFI30 is a novel immune-related target with predicting value of prognosis and treatment response in glioblastoma. Onco Targets Ther 2020;13: 1129-43.
39. Castellanos JR, Purvis IJ, Labak CM, Guda MR, Tsung AJ, Velpula KK, et al. B7-H3 role in the immune landscape of cancer. Am J Clin Exp Immunol 2017;6: 66-75.
40. Hastings KT, Cresswell P. Disulfide reduction in the endocytic pathway: immunological functions of gamma-interferon-inducible lysosomal thiol reductase. Antioxid Redox Signal 2011;15: 657-68.
41. Mair F, Erickson JR, Voillet V, Simoni Y, Bi T, Tyznik AJ, et al. A targeted multi-omic analysis approach measures protein expression and low-abundance transcripts on the single-cell level. Cell Rep 2020;31: 107499.
42. Gan G-L, Liu J, Chen W-J, Ye Q-Q, Xu Y, Wu H-T, et al. The diverse roles of the mucin gene cluster located on chromosome 11p15.5 in colorectal cancer. Front Cell Dev Biol 2020;8: 514.
43. Patel KK, Miyoshi H, Beatty WL, Head RD, Malvin NP, Cadwell K, et al. Autophagy proteins control goblet cell function by potentiating reactive oxygen species production. EMBO J 2013;32: 3130-44.
44. Miller KD, Ostrom QT, Kruchko C, Patil N, Tihan T, Cioffi G, et al. Brain and other central nervous system tumor statistics. CA Cancer J Clin 2021;71: 381-406.
45. Dapash M, Hou D, Castro B, Lee-Chang C, Lesniak MS. The interplay between glioblastoma and its microenvironment. Cells 2021;10: 2257.
46. Oronsky B, Reid TR, Oronsky A, Sandhu N, Knox SJ. A Review of newly diagnosed glioblastoma. Front Oncol 2021;10: 574012.
47. Inda M-D-M, Bonavia R, Seoane J. Glioblastoma multiforme: a look inside its heterogeneous nature. Cancers 2014;6: 226-39.
48. Katoh M, Aids T, Sugimoto S, Suwamura Y, Abe H, Isu T, et al. Immunohistochemical analysis of giant cell glioblastoma. Pathol Int 1995;45: 275-82.
49. Sunayama J, Matsuda KI, Sato A, Tachibana K, Suzuki K, Narita Y, et al. Crosstalk between the PI3K/mTOR and MEK/ERK pathways involved in the maintenance of self-renewal and tumorigenicity of glioblastoma stem-like cells. Stem Cells 2010;28: 1930-9.
50. Olympios N, Gilard V, Marguet F, Clatot F, di FF, Fontanilles M. *TERT* promoter alterations in glioblastoma: a systematic review. Cancers 2021;13: 1147.
51. Kayabolen A, Yilmaz E, Bagci-Onder T. IDH mutations in glioma: double-edged sword in clinical applications? Biomedicines 2021;9: 799.
52. Kozak KR, Moody JS. Giant cell glioblastoma: a glioblastoma subtype with distinct epidemiology and superior prognosis. Neuro Oncol 2009;11: 833-41.
53. Ogawa K, Kurose A, Kamataki A, Asano K, Katayama K, Kurotaki H. Giant cell glioblastoma is a distinctive subtype of glioma characterized by vulnerability to DNA damage. Brain Tumor Pathol 2020;37: 5-13.
54. Temme A, Geiger KD, Wiedemuth R, Biol D, Conseur K, Pietsch T, et al. Giant cell glioblastoma is associated with altered aurora b expression and concomitant p53 mutation. J Neuropathol Exp Neurol 2010;69: 632-42.
55. Hoffman DI, Abdullah KG, McCoskey M, Binder ZA, O'Rourke DM, Desai AS, et al. Negative prognostic impact of epidermal growth factor receptor copy number gain in young adults with isocitrate dehydrogenase wild-type glioblastoma. J Neurooncol 2019;145: 321-8.
56. Shi ZF, Li KK-W, Kwan JSH, Yang RR, Aibaidula A, Tang Q, et al. Whole-exome sequencing revealed mutational profiles of giant cell glioblastomas. Brain Pathol 2019;29: 782-92.
57. Cantero D, Mollejo M, Sepúlveda JM, D'Haene N, Gutiérrez-Guamán MJ, Rodríguez de Lope Á, et al. TP53, ATRX alterations, and low tumor mutation load feature IDH-wildtype giant cell glioblastoma despite exceptional ultra-mutated tumors. Neurooncol Adv 2020;2: vdz059.
58. Galbraith K, Kumar A, Abdullah KG, Walker JM, Adams SH, Prior T, et al. Molecular correlates of long survival in IDH-wildtype glioblastoma cohorts. J Neuropathol Exp Neurol 2020;79: 843-54.
59. Barresi V, Simbolo M, Mafficini A, Martini M, Calicchia M, Piredda ML, et al. IDH-wild type glioblastomas featuring at least 30% giant cells are characterized by frequent RB1 and NF1 alterations and hypermutation. Acta Neuropathol Commun 2021;9: 200.
60. Harabin-Słowińska M, Słowiński J, Konecki J, Mrówka R. Expression of adhesion molecule CD44 in metastatic brain tumors. Folia Neuropathol 1998;36: 179-84.
61. Klank RL, Decker Grunke SA, Bangasser BL, Forster CL, Price MA, Odde TJ, et al. Biphasic dependence of glioma survival and cell migration on CD44 expression level. Cell Rep 2017;19: 668.
62. Ahmadipour Y, Gembruch O, Pierscianek D, Sure U, Jabbarli R. Does the expression of glial fibrillary acid protein (GFAP) stain in glioblastoma tissue have a prognostic impact on survival? Neurochirurgie 2020;66: 150-4.
63. Jung E, Alfonso J, Monyer H, Wick W, Winkler F. Neuronal signatures in cancer. Int J Cancer 2020;147: 3281-91.
64. Jung E, Osswald M, Blaes J, Wiestler B, Sahm F, Schmenger T, et al. Tweety-homolog 1 drives brain colonization of gliomas. J Neurosci 2017;37: 6837-50.
65. Elkamhawy A, Lu Q, Nada H, Woo J, Quan G, Lee K. The journey of ddr1 and ddr2 kinase inhibitors as rising stars in the fight against cancer. Int J Mol Sci 2021;22: 6535.
66. Vehlow A, Cordes N. DDR1 (discoidin domain receptor tyrosine kinase 1) drives glioblastoma therapy resistance by modulating autophagy. Autophagy 2019;15: 1487-8.

67. Becerra-Hernández LV, Escobar-Betancourt MI, Pimienta-Jiménez HJ, Buriticá E. Crystallin Alpha-B overexpression as a possible marker of reactive astrogliosis in human cerebral contusions. Front Cell Neurosci 2022;16: 838551.
68. Kore RA, Abraham EC. Phosphorylation negatively regulates exosome mediated secretion of cryAB in glioma cells. Biochim Biophys Acta 2016;1863: 368-77.
69. Berezovsky AD, Poisson LM, Cherba D, Webb CP, Transou AD, Lemke NW, et al. Sox2 promotes malignancy in glioblastoma by regulating plasticity and astrocytic differentiation. Neoplasia 2014;16: 193-206.
70. Meyer-Puttlitz B, Hayashi Y, Waha A, Rollbrocker B, Bostrom J, Wiestler OD, et al. Molecular genetic analysis of giant cell glioblastomas. Am J Pathol 1997;151: 853-7.
71. Karsy M, Gelbman M, Shah P, Balumbu O, Moy F, Arslan E. Established and emerging variants of glioblastoma multiforme: review of morphological and molecular features. Folia Neuropathol 2012;50: 301-21.
72. Mlecnik B, Tosolini M, Kirilovsky A, Berger A, Bindea G, Meatchi T, et al. Histopathologic-based prognostic factors of colorectal cancers are associated with the state of the local immune reaction. J Clin Oncol 2011;29: 610-8.
73. Wang E, Miller LD, Ohnmacht GA, Mocellin S, Perez-Diez A, Petersen D, et al. Prospective molecular profiling of melanoma metastases suggests classifiers of immune responsiveness. Cancer Res 2002;62: 3581-6.
74. Locy H, Verhulst S, Cools W, Waelput W, Brock S, Cras L, et al. Assessing tumor-infiltrating lymphocytes in breast cancer: a proposal for combining immunohistochemistry and gene expression analysis to refine scoring. Front Immunol 2022;13: 794175.
75. Yu A, Mansure JJ, Solanki S, Siemens DR, Koti M, Dias ABT, et al. Presence of lymphocytic infiltrate cytotoxic T lymphocyte CD3+, CD8+, and immunoscore as prognostic marker in patients after radical cystectomy. PLoS One 2018;13: e0205746.
76. Reyaz N, Tayyab M, Khan SA, Siddique T. Correlation of glial fibrillary acidic protein (GFAP) with grading of the neuroglial tumours. J Coll Physicians Surg Pak 2005;15: 472-5.
77. Takemura M, Gomi H, Colucci-Guyon E, Itohara S. Protective role of phosphorylation in turnover of glial fibrillary acidic protein in mice. J Neurosci 2002;22: 6972-9.
78. Wang H, Zhang L, Zhang IY, Chen X, Da Fonseca A, Wu S, et al. S100B promotes glioma growth through chemoattraction of myeloid-derived macrophages. Clin Cancer Res 2013;19: 3764-75.
79. Zhang L, Liu W, Alizadeh D, Zhao D, Farrukh O, Lin J, et al. S100B attenuates microglia activation in gliomas: possible role of STAT3 pathway. Glia 2011;59: 486-98.
80. Millward TA. Calcium regulation of Ndr protein kinase mediated by S100 calcium-binding proteins. EMBO J 1998;17: 5913-22.
81. Arcuri C, Bianchi R, Brozzi F, Donato R. S100B increases proliferation in PC12 neuronal cells and reduces their responsiveness to nerve growth factor via Akt activation. J Biol Chem 2005;280: 4402-14.
82. Hu Y, Song J, Wang Z, Kan J, Ge Y, Wang D, et al. A Novel S100 family-based signature associated with prognosis and immune microenvironment in glioma. J Oncol 2021;2021: 3586589.
83. Murai T, Miyazaki Y, Nishinakamura H, Sugahara KN, Miyauchi T, Sako Y, et al. Engagement of CD44 promotes Rac activation and CD44 cleavage during tumor cell migration. J Biol Chem 2004;279: 4541-50.
84. Si D, Yin F, Peng J, Zhang G. High expression of CD44 predicts a poor prognosis in glioblastomas. Cancer Manag Res 2020;12: 769-75.
85. Figueroa JM, Carter BS. Detection of glioblastoma in biofluids. J Neurosurg 2018;129: 334-40.
86. Nakagawa H, Yamada M, Kanayama T, Tsuruzono K, Miyawaki Y, Tokiyoshi K, et al. Myelin basic protein in the cerebrospinal fluid of patients with brain tumors. Neurosurgery 1994;34: 825-33.
87. Zavialova MG, Shevchenko VE, Nikolaev EN, Zgoda VG. Is myelin basic protein a potential biomarker of brain cancer? Eur J Mass Spectrom 2017;23: 192-6.
88. Golflnos JG, Norman SA, Coons SW, Norman RA, Ballecer C, Scheck3 AC. Expression of the genes encoding myelin basic protein and proteolipid protein in human malignant gliomas. Clin Cancer Res 1997;3: 799-804.
89. Rozenblum GT, Kaufman T, Vitullo AD. Myelin basic protein and a multiple sclerosis-related MBP-peptide bind to oligonucleotides. Mol Ther Nucleic Acids 2014;3: e192.
90. Nakada M, Minamoto T, Pyko IV, Hayashi Y, Hamada J-I. The pivotal roles of GSK3β in glioma biology. In M Garami, editor. Molecular targets of CNS tumors. London (UK): IntechOpen; 2011. p. 567.
91. Majewska E. AKT/GSK3β signaling in glioblastoma. Neurochem Res 2017;42: 918-24.
92. Wang Y, Zhang Y, Qian C, Cai M, Li Y, Li Z, et al. GSK3β/β-catenin signaling is correlated with the differentiation of glioma cells induced by wogonin. Toxicol Lett 2013;222: 212-23.
93. Rossi G, Redaelli V, Perego P, Ferrari R, Giaccone G, Tagliavini F. Tau mutations as a novel risk factor for cancer-response. Cancer Res 2018;78: 6525.
94. Yang J, Yu Y, Liu W, Li Z, Wei Z, Jiang R. Microtubule-associated protein tau is associated with the resistance to docetaxel in prostate cancer cell lines. Res Rep Urol 2017;9: 71-7.
95. Bonneau C, Gurard-Levin ZA, Andre F, Pusztai L, Rouzier R. Predictive and prognostic value of the tauprotein in breast cancer. Anticancer Res 2015;35: 5179-84.
96. Barbolina MV. Dichotomous role of microtubule associated protein tau as a biomarker of response to and a target for increasing efficacy of taxane treatment in cancers of epithelial origin. Pharmacol Res 2021;168: 105585.
97. Lim S, Kim D, Ju S, Shin S, Cho IJ, Park SH, et al. Glioblastoma-secreted soluble CD44 activates tau pathology in the brain. Exp Mol Med 2018;50: 1-11.
98. Pagano A, Breuzard G, Parat F, Tchoghandjian A, Figarella-Branger D, de Bessa TC, et al. Tau regulates glioblastoma progression, 3D cell organization, growth and migration via the PI3K-AKT axis. Cancers 2021;13: 5818.